COMPARISON OF SEROTONIN$_{1A}$ RECEPTOR DISTRIBUTION AND FUNCTIONAL ACTIVATION IN THE VISUAL CORTEX

A multimodal neuroimaging study combining quantitative molecular and high field functional magnetic resonance imaging in vivo.

Dissertation zur Erlangung des akademischen Grades

"Doktor der gesamten Heilkunde"

Eingereicht von

Florian Gerstl

KLINISCHE ABTEILUNG FÜR BIOLOGISCHE PSYCHIATRIE

Medizinische Universität Wien

Universitätsklinik für Psychiatrie und Psychotherapie

Währinger Gürtel 18-20, 1090 Wien

Betreuung: O. Univ. Prof. Dr. Dr. h.c. Siegfried Kasper

Wien, Juni 2007

1 Vorwort

Zum Gelingen der vorliegenden Arbeit haben viele Menschen beigetragen, die mich bei der Durchführung meiner Arbeit unterstützt und beraten haben. Ihnen sei an dieser Stelle gedankt.

Meinem Betreuer O. Univ. Prof. Dr. Dr. h.c. Siegfried Kasper, an dessen Abteilung ich forschen konnte und der mich mehrmals an die internationale Forschungsgemeinschaft weiterempfohlen und mir somit ermöglicht hat, meinen wissenschaftlichen Horizont beträchtlich zu erweitern.

Ao. Univ Prof. Dipl. Ing. Dr. Ewald Moser danke ich für die Gelegenheit zur Arbeit am Exzellenzzentrum für Hochfeld MR. Die an dieser Einrichtung praktizierte Interdisziplinarität war für mich eine äußerst bereichernde Gelegenheit, wissenschaftlichen Erfahrungsaustausch über die Grenzen meiner eigenen Disziplin hinaus zu betreiben.

Dr. Rupert Lanzenberger, dem ich mein Wissen über PET - Bildgebung verdanke und von dessen umfangreichen neurowissenschaftlichen Kenntnissen ich enorm profitieren konnte, für die Inspiration zu meiner Arbeit, die Gelegenheit, diese in seiner Forschungsgruppe durchführen zu können und ganz besonders für seine Geduld und Sorgfalt bei der Durchsicht meiner Dissertation.

Dipl. Ing. Dr. Christian Windischberger verdanke ich mein gesamtes Wissen über MR Bildgebung, die Durchführung sowie die Analyse funktioneller MR Studien. Mit viel persönlichem Einsatz und großer Begeisterung hat er mir die Faszination der Begegnung zwischen Medizin und Technik vermittelt und mir ermöglicht, mich zwischen beiden Welten zu bewegen.

Den Kollegen am Exzellenzzentrum für Hochfeld MR danke ich für zahllose Tricks und Kniffe im Umgang mit Computern, die meine Arbeit sehr erleichtert haben.

Vielen Dank auch den Kollegen an der Universitätsklinik für Psychiatrie sowie dem PET- Zentrum für die gute Zusammenarbeit.

Mein letzter und tiefster Dank gilt jenen, denen ich die Möglichkeit zu studieren, die Fähigkeit kritisch und interessiert zu denken sowie Rückhalt und Zuhause über die Jahre hinweg verdanke, meinen Eltern und meiner Familie.

2 Summary

Backgrounds: Although there are numerous studies using either PET or fMRI, there is considerable lack of data combining both methodologies to examine the relationship between neuroreceptor distribution patterns and functional organization of the human brain. This relationship, however, seems to be a key factor for understanding the processes underlying neurological and psychiatric disorders. For the serotonergic system, the major inhibitory receptor 5-HT$_{1A}$ shows a distinct topological distribution. Primary sensory areas express very low levels of the 5-HT$_{1A}$ receptor compared to adjacent cortical regions. Here we assessed the relationship of neurochemical cortical borders as determined by PET with the retinotopic organization of the primary visual cortex as indicated by fMRI retinotopy by overlaying parametric receptor distribution maps on structural data.

Aim: The objective of this multimodal neuroimaging study was to combine functional magnetic resonance imaging (fMRI) and positron emission tomography (PET) to investigate the relationship between functional-defined primary and secondary visual areas (V1, V2) and the neurochemical distribution of the 5-HT$_{1A}$ receptor.

Methods: A group of 7 young, healthy subjects was studied using both PET and fMRI. Quantitative data of the 5-HT$_{1A}$ receptor was acquired using a GE Advance PET scanner and the radioligand [^{11}C]WAY-100635. Final reconstructed image resolution was FWHM=4.36mm at the centre of the field (128x128, 35 slices). The parametric distribution of the 5-HT$_{1A}$ receptor was calculated using the SRTM and PMOD2.7. Functional imaging was performed at 3 Tesla (Bruker Biospin, Germany) acquiring ten oblique axial slices centered on the calcarine sulcus. Subjects performed a visual paradigm involving the presentation of two opposing checkerboard-wedges in a "propeller" configuration. By means of this stimulus activation specific to the polar properties of the visual field was registered on the cortex. A cortical surface model was constructed from structural MR scans and flattened with the CARET software suite. PET and fMRI data was brought into the same stereotactical space as the structural MRI scans, functional data was projected on the cortical surface employing multiple mapping algorithms and functional areas were delineated.

Results: Comparison of V1/V2 ratios achieved from 14 hemispheres by multiple mapping algorithms exhibited a 5-HT$_{1A}$ receptor distribution ratio normally distributed around 0.8. This figure is in good agreement with data available from post-mortem studies

Conclusion: In post-mortem studies, area-specific expression patterns of different neuroreceptor subtypes have been used for the neurochemical differentiation of brain areas. Our data show that the 5-HT$_{1A}$ receptor distribution pattern can be used to define the primary visual cortex by a neurochemical marker in humans in vivo verified by retinotopic mapping with fMRI. The method of neurochemical delineation of functional areas in vivo, as demonstrated in this thesis, yields numerous promising possibilities for future neuroscientific research.

3 Zusammenfassung

Hintergrund: Trotz des Vorliegens zahlreicher PET bzw. fMRI Studien gibt es einen Mangel an vergleichenden Untersuchungen hinsichtlich des Zusammenhanges neurochemischer Parameter einzelner Hirnareale mit der dort lokalisierten Funktion. In diesem Zusammenhang scheint allerdings ein Schlüssel zum Verständnis neurologischer und psychiatrischer Erkrankungen zu liegen. Der wichtigste inhibitorische Neurotransmitter-Rezeptor des serotonergen Systems, der 5-HT$_{1A}$ Rezeptor, weist eine spezifische topologische Verteilung im Gehirn auf. Primär sensorische Areale weisen gegenüber benachbarten Regionen eine besonders niedrige Dichte dieses Rezeptortyps auf. In der vorliegenden Studie wurde dieser neurochemische Unterschied anhand des primär visuellen Kortex, der unter Anwendung eines auf retinotopen Prinzipien basierenden fMRI- Experimentes abgegrenzt wurde, untersucht.

Ziel: Ziel der vorliegenden Studie mittels Kombination von fMRI und PET die Beziehung zwischen funktionell definierten primär und sekundär sensorischen Arealen im visuellen Kortex und der Verteilung des 5-HT$_{1A}$ Rezeptors in diesen Arealen zu untersuchen.

Methoden: 7 gesunde Probanden (6 Frauen, 1 Mann, Durchschnittsalter: 24,4 Jahre) nahmen an der Studie teil. Für den angestrebten multimodalen Vergleich unterzogen sich die Probanden sowohl PET als auch fMRI Messungen. Für die quantitative Darstellung der Verteilung des 5-HT$_{1A}$ Rezeptors gelangte der Radiotracer [^{11}C]WAY-100635 in einem GE Advance PET Scanner zum Einsatz. Die parametrische Verteilung des Rezeptors wurde unter Anwendung des *simplified reference tissue models* (SRTM) modelliert. Die funktionellen Magnetresonanzmessungen wurden bei 3 Tesla Feldstärke (Bruker Biospin, Deutschland) durchgeführt. Zehn Schichten parallel zum Sulcus calcarinus, der anatomischen Leitstruktur der Sehrinde, wurden zu 128 Zeitpunkten registriert (TR= 1 Sek.). Durch das den Probanden während der Messungen präsentierte visuelle Stimulationsparadigma konnte Aktivierung spezifisch für die polare Repräsentation im visuellen Kortex registriert werden, anhand derer eine Abgrenzung zu anderen funktionellen Gebieten ermöglicht wurde. Die so erhaltenen Daten wurden auf einem Oberflächenmodell eines ebenfalls durchgeführten strukturellen Scans des Gehirns anhand mehrerer Projektionsalgorithmen visualisiert.

Ergebnisse: Anhand der V1/V2 Vergleiche, errechnet mithilfe multipler ROI-Definitionen und Projektionsalgorithmen konnte das Verhältnis des 5-HT$_{1A}$ Rezeptors zwischen dem primären und sekundären visuellen Kortex als um 0,8 normalverteilter Wert bestimmt werden. Dieses Ergebnis steht im Einklang mit autoradiographischen post-mortem Daten dieser Hirnregion.

Konklusion: Die Parzellierung der Hirnrinde anhand neurochemischer Verteilungsmuster war bis dato der autoradiographischen Untersuchung histologischer Schnitte vorbehalten. Anhand der gewonnenen Daten konnte in dieser Studie gezeigt werden, dass sich der 5-HT$_{1A}$ Rezeptor als neurochemisches Differenzierungskriterium für den primär visuellen Kortex in vivo eignet. Die Anwendung dieses Kriteriums zur in vivo Parzellierung funktioneller Areale erscheint uns als viel versprechende Methode für unsere zukünftige neurowissenschaftliche Forschungstätigkeit.

4 Table of Contents

5 Introduction

Over the last two decades, enormous developments in the field of medical imaging have enabled neuroscientists to gain a deeper insight into the functioning of the central nervous system (Kasper et al. 2002). The arrival of high-resolution imaging techniques capable of exploring structural, physiological and chemical parameters in the living human brain fundamentally opened up the field of brain mapping *in vivo*.

Cerebral cortex structure has been parcellated since the very beginning of neuroscience research. Classification criteria included gross anatomy, myelinisation, neuron density and arrangement or connectivity between neurons. With the advent of molecular imaging technology an additional criterion for delineations in the cortex has become available, namely its neurochemical structure, in particular the density of the different types of neurotransmitter-receptors or transporters and their subtypes. Zilles performed autoradiography studies of post-mortem brains and compared the receptor binding of 20 different neurotransmitter receptors with functional data acquired from other studies by morphing the individual brains into the same spatial reference system (Zilles, Palomero-Gallagher et al. 2002). He found a strong correlation between neurochemical and structural properties of the cortex and hypothesized that a correlation between functional and neurochemical properties in the cortex is very likely to exist.

The border between the primary (BA17/ V1) and secondary (BA18/V2) visual cortex is especially well defined by the classification criteria mentioned above. The myeloarchitectonic border is characterized by the presence of the stripe of Gennari in V1 but not in V2. Cytoarchitectonically layer IV of the cortex looses its subdivision (IVa, IVb, IVc) on the transitory from V1 to V2 (Brodmann 1909). Functionally the representation of the vertical meridian in the visual field

characterizes the outermost parts parallel to the calcarine sulcus of both V1 and V2 and thus their bordering region. Finally, a neurochemical distinction between V1 and V2 based on 5-HT$_{1A}$ receptor distribution in post-mortem brains has been indicated in Scheperjans, Palomero-Gallagher et al. 2005 by [3H]-8-OH-DPAT autoradiography.

In humans, the optical sense is of exceptional importance, therefore the investigation of the visual system has always been an area of prime interest for neurosciences. In the study presented here several state of the art neuroimaging methods have been employed to reveal evidence for the tight entanglement of physiological processes with their underlying structures in the occipital cortex

Beginning with the description of the aim of this study and the definition of the hypotheses tested, a short overview of the serotonergic as well as the visual system, and the linkage between both systems examined in this study, will be presented in this thesis. Further the sophisticated methods of neuroimaging applied here as well as their underlying mechanisms will be introduced in theory in chapter 8 (Background). Details of the practical application of these procedures are summarized in the Methods section. Findings of the study are quantified in the Results section which forms the initial point for the following Discussion evaluating the relevance of those findings and the methods applied for neuroscientific research.

6 Aim

The objective of this multimodal neuroimaging study was to combine functional magnetic resonance imaging (fMRI) and positron emission tomography (PET) to investigate the relationship between functional-defined primary and secondary visual areas (V1, V2) and the neurochemical distribution of the 5-HT$_{1A}$ receptor. The distribution patterns of neurotransmitter receptor subtypes "may reflect the cyto- and myeloarchitectonical as well as the functional organisation of the cortex" (Zilles, Palomero-Gallagher et al. 2002). As the first of its kind this study is aimed towards verifying this hypothesis in healthy humans *in vivo*, comparing the 5-HT$_{1A}$ distribution measured by PET and functional retinotopic maps obtained with fMRI in the same subjects.

7 Hypotheses

1. The serotonin$_{1A}$ receptor binding measured by PET and the radioligand [*carbonyl*-^{11}C]-WAY-100635 differs significantly between primary and secondary visual areas (V1 and V2)

2. Functional areas defined by fMRI can be delineated using neurochemical maps of receptor distribution indicating a functional relationship between receptor distribution, brain structure and neural activity.

8 Background

8.1 Serotonergic System

The monoamine neurotransmitter **serotonin** (**5-hydroxytryptamine**, or **5-HT**) is synthesized in living cells by the hydroxylation and decarboxylation of the amino acid tryptophan. It was first isolated by Maurice Rapport in 1948 (Rapport, Green et al. 1948) and named to indicate its ability to affect vascular smooth muscle tone. Most of the serotonin found in the human body is located in enterochromaffine cells in the intestine where it mediates secretory and peristaltic reflexes and, via vagal afferences can also trigger emesis. Other sites where serotonin can be found include mast cells and blood platelets.

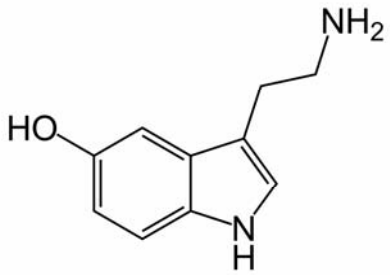

Figure 1. chemical structure of the monoamine neurotransmitter 5-hydroxytryptamine (serotonin)

The amount of serotonin in the central nervous system accounts for about 1-2% of total serotonin abundance in the human organism. The majority of serotonergic neurons is located in the raphe nuclei in the brainstem. They project to motor and autonomous systems in the spinal cord and to the whole cortex and subcortical brain areas, and are also involved in hypothalamic regulation of functions such as cardiovascular and respiratory activity, thermoregulation, sleep, appetite and emesis (Struder and Weicker 2001).). Furthermore, affective (Baldwin and Rudge 1995) and and cognitive brain functions (Buhot, Martin et al. 2000), experience significant regulation and modulation by the serotonergic system.

At least fourteen different receptors for serotonin are known and are expressed in varying concentrations in distinct functional brain areas. Both excitatory and inhibitory neurotransmission is provided by serotonin receptor subtypes. The most important receptor subtype mediating inhibitory neurotransmission is subtype 1A. Its central role in the serotonergic system of the brain and the availability of a highly specific and selective radiotracer for labelling this receptor subtype make this receptor an important target for molecular neuroimaging of the serotonergic system.

8.1.1 The 5-HT$_{1A}$ Receptor

The G-protein-coupled 5-HT$_{1A}$ receptor belongs to the family of adenylyl cyclase inhibiting 5-HT$_1$ receptors. Besides the A subtype, B, D, E and F subtypes exist. Due to a different mechanism of action the 5-HT$_{1C}$ receptor is associated with the 5-HT$_2$ group. As a G- protein coupled receptor the 5-HT$_{1A}$ receptor is located in the cellular membrane and possesses seven membrane spanning domains (Shih, Yang et al. 1991). Activation of 5-HT$_{1A}$ receptors causes hyperpolarization of the neuron by triggering voltage gated K+ channels.

Postsynaptic 5-HT$_{1A}$ receptors are located mainly on glutaminergic and GABAergic neurons, achieving high concentrations in several cortical and subcortical areas especially in the limbic system (Varnas, Halldin et al. 2004). The concentration of 5-HT$_{1A}$ in primary sensory areas, such as the primary visual cortex which is the focus of this study, is generally low. Even lower concentration are found in the cerebellum which is therefore commonly used as reference region for quantification with PET (Varnas, Halldin et al. 2004). Furthermore, 5-HT$_{1A}$ receptors located in the raphe nuclei act as presynaptic autoreceptors providing negative feedback for firing serotonergic neurons and therefore regulating serotonergic firing of neurons in the raphe region and release in cortical areas (Hamon, Lanfumey et al. 1990).

The 5-HT$_{1A}$ receptor distribution is not homogeneous within the cortex and there are huge differences in the 5-HT$_{1A}$ receptor level between primary sensory and secondary cortical areas (Varnas, Halldin et al. 2004). Therefore, these clear topological differences of the 5-HT$_{1A}$ receptor distribution can be used for parcellation of cortical areas. Receptor distribution patterns (Zilles, Palomero-Gallagher et al. 2002), myeoloarchitectonic and cytological patterns (Amunts, Malikovic et al. 2000) have been used in post-mortem brains for parcellation of the cortex. However, it is not clear if the cortical segregation based on receptor distributions in post-mortem brains is correlating with functional parcellations based on fMRI. Here, we used the 5-HT$_{1A}$ receptor distribution in visual areas to test the concordance of neurochemical and functional parcellation.

Hippocampus	6.19 ± 0.98
Anterior cingulated cortex	5.29 ± 0.84
Amygdala	5.54 ± 0.8
Raphe nuclei	4.23 ± 0.8
Insular cortex	5.63 ± 0.84
Occipital lobe	3.28 ± 0.58

Table 1. invivo measured BP values in selected ROIs, adapted from Rabiner, Messa et al 2002

8.2 The neuronal basis of visual perception

The exceptional importance of visual perception for primates in general and humans in particular is reflected by the size and number of areas involved in the process of vision. About 30 distinct visual areas have been described so far (Felleman and Van Essen 1991).

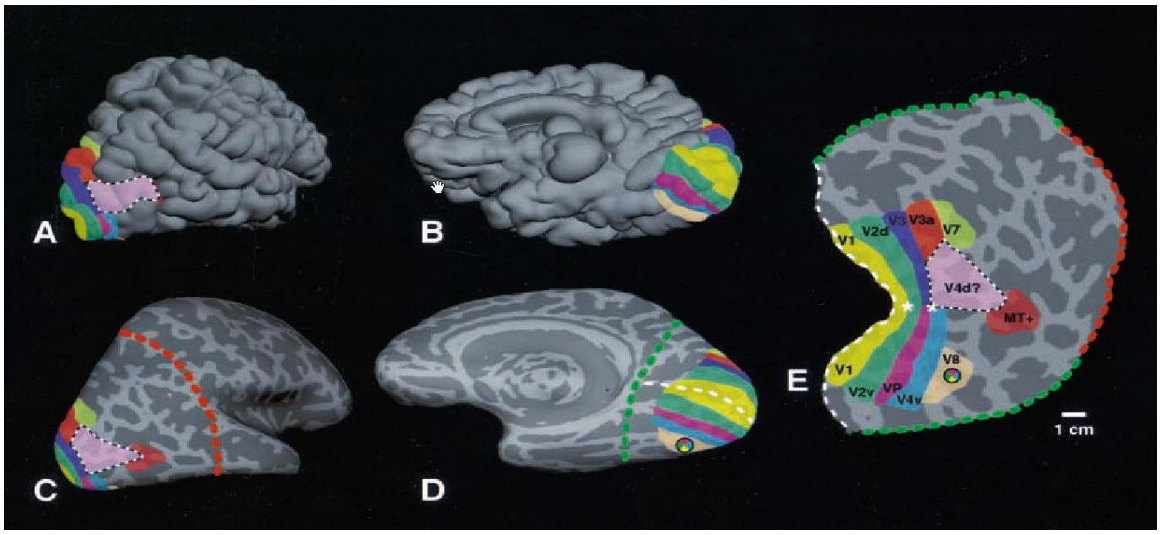

Figure 2. Localization of functional areas of the visual system. A and B show a lateral and ventral view of the areas located at the occipital pole of a right cerebral hemisphere. C and D are their corresponding inflated surface models. The flattened representation (E) includes the names of the visual areas that are assigned different colors in this display. Reproduced from Tootell and Hadjikhani 2001

8.2.1 Anatomy and function of the primary visual cortex (V1)

Similar to other sensory modalities in the brain, the region where visual information first enters neocortical processing is denoted as primary visual cortex. This earliest visual area, also referred to as V1 has its structural equivalent in the anatomically defined striate cortex or Brodmann's area 17 (Bridge, Clare et al. 2005; Wohlschlager, Specht et al. 2005). Interestingly, V1 area shows considerable variability across subjects, as well as intra-subject variability between hemispheres (Amunts, Malikovic et al. 2000).

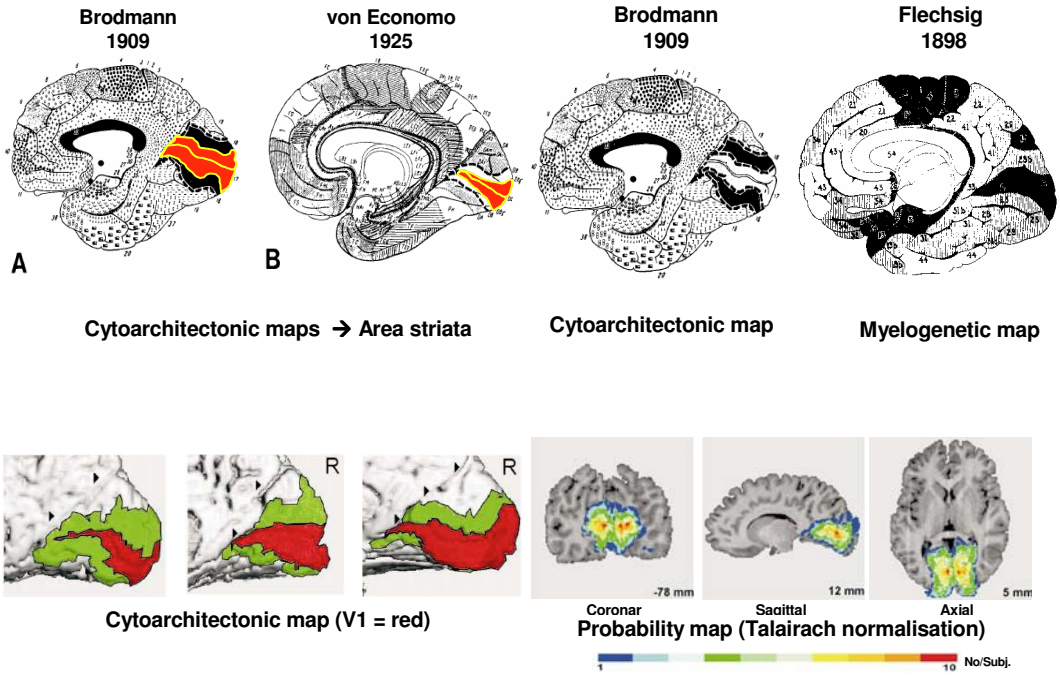

Figure 3. The upper two images show the primary visual cortex as displayed on classical maps parcellating the human brain. The lower two images demonstrate the variability of this area as demonstrated by a probabilistic approach by K. Amunts. reproduced from: Amunts et al. 2000

The name "striate cortex" derives from a prominent stripe of myelinated axons in layer four, the stria of Gennari.

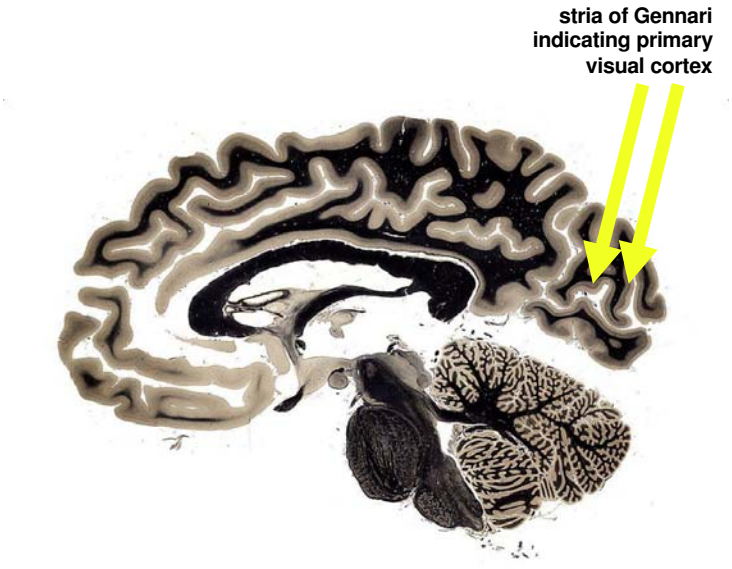

Figure 4. Parasaggital histological slice of human brain with clearly visible striate cortex.

In humans the primary visual cortex has a thickness of about three to five millimetres between pial surface and the white matter boundary. Its vertical structure is histologically and functionally divided in six layers following the general classification scheme of the neocortex.

8.2.2 Secondary visual area (V2)

Visual area V2 is the second major area in the visual cortex, and the first region within the visual association area. It receives strong feedforward connections from V1 and has strong projections to V3, V4, and V5. It also sends strong feedback connections to V1. The first exhaustive description of the connection architecture between V1 and V2 was published by Livingstone and Hubel in 1988. They also described the partial segregation of the P- and M-pathways which remains throughout V2.

Functionally and anatomically, V2 is split into four quadrants, a dorsal and ventral representation in the left and right hemisphere, respectively. Altogether, these four regions maintain the complete map of the visual field as described for V1 above. Some of the functional structures found in primary visual cortex are also present in V2. Cells are tuned to simple properties such as orientation, spatial frequency, and color. Responses of most V2 neurons are, however, also modulated by more complex properties, such as the orientation of illusory contours and whether the stimulus is part of the figure or the ground (Qiu and von der Heydt 2005).

8.2.3 Higher visual areas

Various other extrastriate areas of the visual system besides V2 have been described in the literature. These regions include the middle temporal area (MT), V3 and V4, and are attributed to the processing of distinct modalities as motion (hMT or V5) or colour perception (V4).

8.2.4 Retinotopy

Throughout the cerebral cortex a widespread principle of organization is an arrangement of functional areas replicating the topology of the sensory fields. Primary motor areas as well as various sensory modalities are structured according to their topologic properties. Accordingly, the human visual system maintains a topologically organized map of spatial information received from the retina up to the level of V2 at least. In V1 this map is very precise as even blind spots are mapped to the primary visual cortex (Tootell, Hadjikhani et al. 1998).

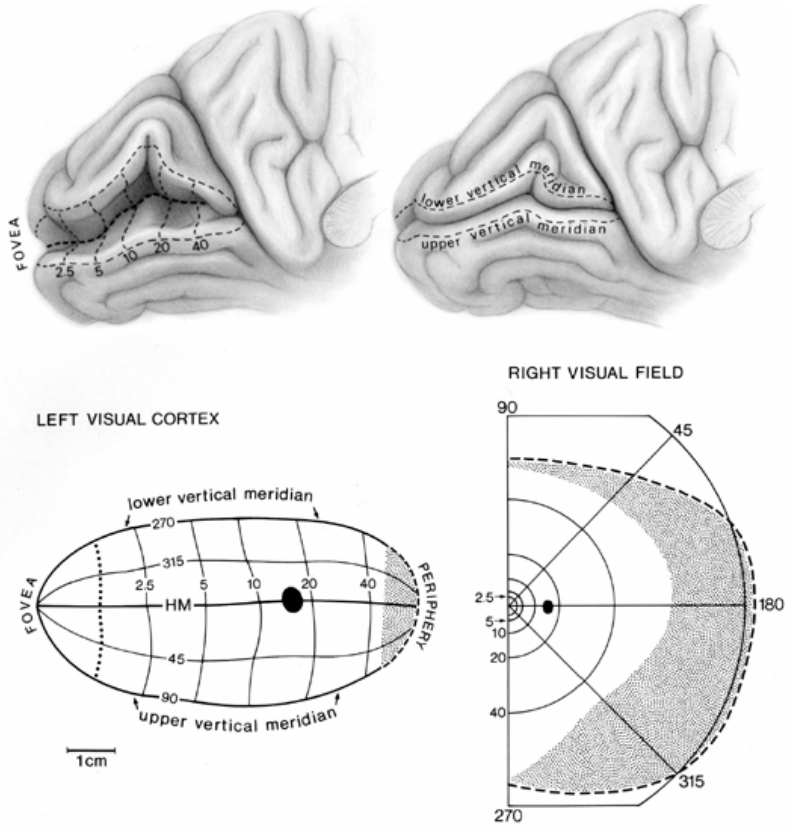

Figure 5 Retinotopic map of the human striate cortex
Upper right shows left ocipital lobe, with most of striate cortex buried in the calcarine fissure. Upper left shows the fissure opened, with distance (eccentricity) from the fovea (center of gaze) marked in degrees. The horizontal meridian (HM) runs roughly along the base of the fissure. Lower left shows the map, removed from the calcarine fissure and flattened. Dots depict occipital pole; the central 1° is located on the exposed lateral convexity, although this varies from person to person. Note the magnification of central vision. Dark oval = blind spot, stippled zone = monocular crescent. From: Horton & Hoyt, Arch Ophthal. 109:861, 1991. (reproduced from http://www.ucsf.edu/hortonlab/ResearchProgram.html)

The lower and upper visual quadrants are represented in the upper and lower calcarine banks of the contralateral hemisphere, the horizontal meridian separating the quadrants lying at the base of the calcarine sulcus. Eccentricity of the visual hemifield is mapped along the calcarine sulcus, the foveal representation being represented at the occipital pole. About 55% of the surface area of primary visual cortex is devoted to the representation of the central 10 degrees of vision, where the highest visual acuity is achieved (Adams and Horton 2003). This overrepresentation of central vision is referred to as cortical magnification.

In secondary visual cortex the upper quadrant of the visual field is represented in the ventral part of V2 (V2v) with the upper vertical meridian being situated at the border to V1 and its horizontal meridian positioned at the border to V3 and other areas. The opposite applies to dorsal V2 (V2d) keeping the retinotopic representation for the lower quadrant of the visual hemifield.

These retinotopic maps can be investigated in a single subject *in vivo* using fMRI. Applying visual stimuli in the form of rotating wedges and expanding rings allows delineation functional retinotopic areas engaged in the different aspects of visual perception (Engel, Rumelhart et al. 1994; DeYoe, Carman et al. 1996; Tootell, Hadjikhani et al. 1998).

8.3 Positron Emission Tomography (PET)

8.3.1 Backgrounds of Positron emission tomography

Positron emission tomography (PET) is an imaging technique in nuclear medicine broadly used in research and clinical routine. The basic principle of PET is based on the detection and visualisation of the distribution of a radioactive tracer substance in living organisms. Structural as well as biochemical and physiological attributes can be measured.

For *in vivo* applications in humans, PET offers the unique possibility to visualize processes as regional blood flow or regional rates of metabolism. This is widely applied in clinical oncology in the search for tumours and metastases.

Another important application for PET is the quantification and localization of receptors, transporters, enzymes and other proteins in the living organism, provided that a selective radioligand for the molecule in focus is available.

Due to substantial requirements on technical equipment and qualified manpower, receptor-specific PET is a very expensive technique and still remains a method reserved for carefully selected groups of subjects.

8.3.2 Principles of PET

The principal concept behind positron emission tomography is the indirect detection and localization of a type of nuclear decay resulting in the emission of an elementary particle with an electric charge of +1, a spin of ½ and the mass of an electron. This specific type of nuclear decay is referred to as "beta plus (β^+) decay" and the resulting antimatter counterpart of an electron is called positron (e^+). Isotopes which undergo β^+ decay and thus are suitable e^+-sources include carbon-11, nitrogen-13, oxygen-15 and fluorine-18. To generate these isotopes the corresponding non radioactive elements are bombarded with protons in a circular particle accelerator, a cyclotron. The main physical properties of isotopes used in PET are summarized in Table 2.

Once emitted in a decay process, a positron will, after leaving the nucleus, collide almost immediately, i.e. within a few millimetres, with its negatively charged counterpart, e^- (the electron) resulting in the annihilation of both particles. The distance a positron is able to travel before annihilation is called the β+ range which depends on the positron energy and on the tissue in which the process takes place. β+ energy varies between the radio-isotopes used.

	^{11}C	^{13}N	^{15}O	^{18}F
Half life (min):	20	10	2	110
Nuclear reaction:	$^{14}N(p,\alpha)\rightarrow^{11}C$	$^{16}O(p,\alpha)\rightarrow^{13}N$	$^{14}N(d,n)\rightarrow^{15}O$	$^{18}O(p,n)\rightarrow^{18}F$
Mode of decay	$\beta+$ (100 %)	$\beta+$ (100 %)	$\beta+$ (100 %)	$\beta+$ (97 %)
Maximum specific radioactivity (Ci/mmol):	9.2×10^6	1.9×10^7	9.1×10^7	1.7×10^6
Maximal energy (MeV)	0.97	1.20	1.74	0.64
Effective biological dose-equivalent/100 MBq tracer	0.4 mSv	0.25 mSv	0.1 mSv	2.5 mSv
$\beta+$ range (mm)	4	5	8	2

Table 2. Main Features of the Most Frequently Used Radionuclides Isotope, adapted from Halldin (Halldin, Gulyas et al. 2001)

The annihilation process results in two gamma-photons of each 511 keV. Due to the conservation of energy and momentum, these photons move in nearly opposite directions (180° ±0.3°) away from the site of annihilation. The resulting line of response (LOR) is derived from the detection of the two gamma-quantums in the PET-scanner at the same time, the so-called coincidence detection. In the PET-scanner, γ-quantum detection is achieved by scintillation counters, which basically consist of a scintillator crystal connected to a photomultiplier (PM).

Each γ–quantum entering the crystal triggers the emission of a photon which hits the photo cathode of the connected PM. Inside the PM, single photo-electrons are then emitted and accelerated by high voltage. These electrons will hit a so-called dynode, detaching a large number of electrons which are again accelerated. This process is repeated several times to obtain a stream of electrons, large enough to be registered with appropriate electronics.

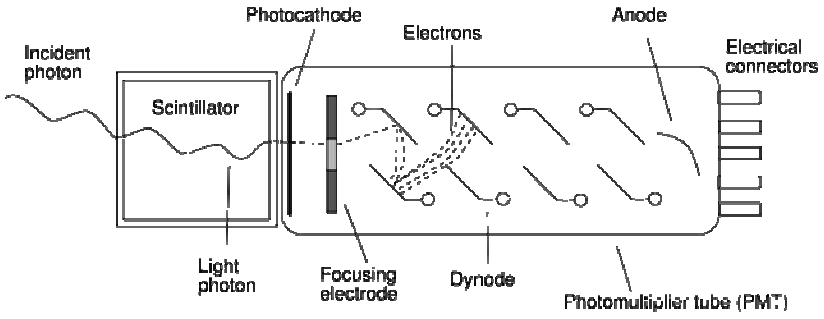

Figure 6. Photomultiplier (from http://commons.wikimedia.org/wiki/Image:Photomultipliertube.svg)

Only coinciding events are registered, i.e. events where the time window is as narrow as typically 10 ns. Besides the described (and wanted) true coincidence, two other types of coincidence can occur: scattered and random coincidences. Scatterd coincidences are a result of the interaction of photons with matter, the so-called Compton scattering, resulting in a wrong line of response from one single annihilation. In contrary, random coincidence is the random coregistration of two distinct annihilation processes within the coincidence-window of 10 ns.

By adding further detector rings to the scanner the resolution of the scan can be enhanced by reducing the rate of not coinciding detections. This PET detector extension is called 3D mode.

A very recent development are scanners, which measure the time difference between the detection of two coincident gamma rays. This technique is being developed in order to not only register the LOR but be able to localize the origin of the annihilation process directly. This is considered to allow faster and better image acquisition than relying on elaborate iterative image reconstruction algorithms needed to solve the inverse problem of reconstructing an image from lines of response (Muehllehner and Karp 2006).

8.3.3 Spatial Resolution limitations in PET

Due to the few millimetres a positron is able to travel before its annihilation, the LOR is recorded not exactly at the origin of the positron emission. This sets a physical border on the maximum image resolution achievable. When using [*carbonyl*-^{11}C]-WAY-100635 as a tracer this limitation of spatial resolution is set about 2mm while the effective achievable resolution lies around 4-5 mm.

8.3.4 In vivo imaging with tracer substances

To conduct a PET scan a tracer substance that has a β+ emitting isotope integrated in its chemical structure is administered to the subject, usually by intravenous blood injection.

When taking into consideration a tracer substance for application in in vivo imaging, several prerequisites have to be fulfilled: the tracer and the radionuclide used as label detectable with PET or SPECT should form a stable complex, the tracer should be sufficiently affine and highly selective for the receptor of interest while exhibiting low non-specific binding to tissue not containing the receptor targeted. The substance should permeate rapidly through the blood-brain barrier permitting quick accessibility of the tracer to its target. The number of metabolites of a labeled ligand should be low and metabolites should underlie a rapid clearance. On the contrary, systemic metabolites should be polar and thus be unable of passing the blood-brain barrier (Heiss and Herholz 2006)**.** An overview of common radiotracers in PET is presented in Table 3.

Tracer	Abbreviation	Target
^{11}C-Cocaine, ^{11}C-methylphenidate		DAT
^{11}C-Nomifensine		DAT
^{11}C-WIN-35428, ^{11}C-PE2I		DAT
^{18}F-2ß-Carbomethoxy-3ß-(4-fluorophenyl)tropane	CFT	DAT
^{11}C-Dihydrotetrabenazine	DTBZ	VMA T_2
^{11}C-SCH-23390		D_1
^{11}C-*N*-Methylspiperone	NMSP	D_2, 5-H T_2
^{18}F-*N*-Methylspiperone		
^{18}F-Fluoroethylspiperone	FESP	D_2, 5-H T_2
^{11}C-Raclopride	RAC	D_2
^{18}F-Fallypride		D_2
N-1-^{11}C-Propylnorapomorphine		D_2 (agonist)
^{11}C-L-Deprenyl		MAO-A
^{11}C-*N*-Methyl-4-piperidylbenzilate	NMPB	Muscarinic receptors
N-^{11}C-Methylpiperdin-4-yl-propionate	MP4P, PMP	AchE
N-^{11}C-Methyl-4-piperidyl-acetate	MP4A, AMP	AchE
^{11}C(+)-McN5652		5-HTT
^{11}C-3-Amino-4-(2-dimethylaminomethyl-phenylsulfanyl) benzonitrile	DASB	5-HTT
^{11}C-WAY-100635	WAY	5-H T_{1A} receptor
^{18}F-Altanserin		5-H T_{2A} receptor
^{11}C-Flumazenil	FMZ	$GABA_A$/benzodiazepine receptors
^{11}C-PK-11195	PK	Peripheral benzodiazepine receptors
^{11}C-Carfentanyl		Opioid μ receptor
^{11}C-Diprenorphine	DPN	Opioid receptors
^{18}F-Cyclofoxy		Opioid receptors
^{18}F-CPFPX, ^{11}C-MPDX		Adenosine A_1 receptor

Table 3. Selected Receptor tracers, reproduced from (Heiss and Herholz 2006) DAT = dopamine transporter; $VMAT_2$ = vesicular monoamine transporter type 2; D1 = dopamine 1 receptor; D2 = dopamine 2 receptor; 5-HT = 5-hydroxytryptamine (serotonin) receptor; 5-HTT = 5-hydroxytryptamine (serotonin) transporter; MAO-A = monoamino-oxidase A; AChE = acetylcholinesterase; GABA = γ-aminobutyric acid receptor.

8.3.5 The radioligand [carbonyl-^{11}C]-WAY-100635

For the purpose of evaluating 5-HT$_{1A}$ receptor binding in the human brain the selective antagonist WAY-100635 (N-[2-[4-(2-methoxyphenyl)-1-piperazinyl]ethyl)-N-(2-pyridinyl) cyclohexanecarboxamide trihydrochloride) can be labelled with the radioactive carbon isotope ^{11}C. This highly specific and selective high-affinity radioligand for the 5-HT$_{1A}$ receptor has been successfully used in various studies (Gunn, Sargent et al. 1998; Rabiner, Messa et al. 2002; Turner, Rabiner et al. 2005; Lanzenberger, Mitterhauser et al. 2007). The standard procedure for the synthesis of this tracer was first implemented by Pike et al (Pike, McCarron et al. 1996) and optimized by Wadsak et al (Wadsak 2007).

8.3.6 Kinetic modelling and Simplified Reference Tissue Model

Kinetic modelling establishes a mathematical link between radioactivity time courses measured in a PET scan at a certain location on the one hand and the presumed distribution of neurotransmitter receptors on the other. When relating measured activity to the underlying neurochemical properties several parameters must be taken into account: plasma levels of the tracer substance, binding and dissociation constants for the radiotracer, as well as the concentration of ligands competing with the radiotracer at the receptor binding site. Most often, a compartmental system is assumed for tracer kinetic modelling in PET studies. The receptor binding potential (RBP) or the distribution volume reflects the receptor density in the region investigated.

In case of the 5-HT_{1A} receptor binding potential the simplified reference tissue model (SRTM) is frequently used for quantification (Lammertsma and Hume 1996)) as it has been shown in some studies to be advantageous to arterial sampling approaches (Gunn, Sargent et al. 1998). This SRTM model allows the estimation of the receptor binding potential using the cerebellum as reference region and applying the formula

$$BP = \frac{B_{\max} * f_2}{K_D(1 + \sum \frac{f_i}{K_i})}$$

where B_{max} denotes the maximum concentration of binding sites, f2 means the free fraction of unbound radio tracer, K_D the dissociation constant for the radio-tracer, and f_i and K_i represent the free concentration of competing endogenous ligand and its dissociation constant, respectively (Rabiner, Messa et al. 2002).

8.4 MRI Basics, Structural and Functional MRI

8.4.1 Structural magnetic resonance imaging (MRI)

Despite the fact that magnetic properties of the nucleus of an atom are exploited for imaging purposes in nuclear magnetic resonance (NMR), the adjective "nuclear" had been abandoned very early and replaced by the term magnetic resonance imaging (MRI) in clinical application to avoid negative connotations of the word "nuclear". Despite its lack of physical accuracy, for namely electron spin resonance (ESR) could as well be added under MRI the widely accepted term "MRI" will be used in this thesis for describing nuclear magnetic resonance imaging.

One basic principle behind MRI is the fact that atomic nuclei with an odd number of protons and/or and odd number of neutrons possess a nonzero nuclear spin $\vec{I}$. Nucleons, even if the show no overall electric charge, are composed of electrically charged quarks. Due to this inner structure, all nucleons show a magnetic moment $\vec{\mu}$.

The most common nucleus with this property is the hydrogen nucleus ^{1}H which consists of a single proton. In the thermal equilibrium state, without any external magnetic field, there is no preferred direction for the orientation of the magnetic moments in a volume of interest. Accordingly, no overall magnetic momentum is observable. For quantum mechanical reason, spins -½ particles (like the ^{1}H nucleus) that are placed in an external magnetic field B_0 may show two and only two spin orientations: either parallel or antiparallel to B_0. Both states exhibit different energy levels (so-called nuclear Zeeman effect). The parallel state is associated with less potential energy and, thus, is the energetically favoured, i.e. there is a surplus of spins with parallel orientation.

Magnetic moments are not static but precess around the external magnetic field at a specific rate, the Larmor frequency which is given by:

$$\omega = \gamma * B$$

γ is a substance specific constant denoted as the gyromagnetic ratio. The Larmor frequency is depending linearly on the magnetic field strength B_0. Table 4 gives an overview on ω for some common nuclei:

Nucleus	**$\gamma / 2\pi$ (MHz/ T)**
^{1}H	42.576
^{7}Li	16.546
^{13}C	10.705
^{14}N	3.0766
^{15}N	4.3156
^{17}O	5.7716
^{23}Na	11.262
^{31}P	17.235

Table 4. Gyromagnetic ratio for common nuclei

For protons that are used in MR- Imaging the Larmor frequency is 42.58 MHz per Tesla field strength of B_0.

A radio frequency (RF) pulse with frequency ω_0 applied perpendicular to the direction of B_0 will cause an additional precession movement around the RF pulse axis. A RF pulse with enough energy to rotate the spins into the plane perpendicular to B_0 is referred to as a 90° pulse. Part of this RF energy is emitted back when the spin ensemble returns to its original state of thermal equilibrium, i.e. oriented along the axis of the static magnetic field B_0, and is received by RF coils. The signal recorded during this relaxation process is called "free induction decay" or FID and represents the basis for all MR measurements.

The time the relaxation process takes is tissue specific and this property is utilized for most clinical applications of MRI. The image contrast between various types of tissue is strongly dependant on sequence parameters (eg TE, TR), which may be varied in a wide range. This feature allows MR sequences to be tailored for specific applications and explains the tremendous clinical value of MR examinations, making them superior to most other medical imaging methods available.

In the brain for example white matter, cortical and subcortical grey matter and cerebrospinal fluid have significantly different T_1 relaxation times (WM: 573ms, GM: 991ms, CSF: 2063ms at 1,5 Tesla B_0 field strength) allowing a clear differentiation of those tissue types via T_1 weighting.

The relaxation process is characterized by two distinct occurrences, both described by different relaxation constants. The longitudinal relaxation constant or T_1 reflects the spin ensemble's return to thermal equilibrium, while the transversal or T_2 relaxation refers to as the loss of phase coherence in the transversal plane, i.e. perpendicular to the direction of B_0.

T_1-relaxation is also denoted as spin-lattice relaxation as the spins exchange energy with their environment known as lattice in solid state physics. In contrast, the transverse relaxation time T_2 describes a loss of net magnetization in the x-y plane which is a result of magnetic interaction between the spins, leading to the label "spin-spin relaxation" for T_2. Inhomogenities of the external magnetic field account for additional loss of phase coherence with the extent of dephasing depending on the degree of inhomogenity. The combination of the two dephasing mechanisms is referred to as T_2*.

The two relaxation processes occur simultaneously, with T_1 being longer then T_2 in biological tissues. As a consequence different pulse sequences are employed to generate data which are differentially weighted by the two relaxation parameters to

take advantage of different contrasts and physiological phenomena observable at these sequences in imaging (see fMRI).

The extraction of spatial information from a volume sample using nuclear magnetic resonance phenomena, magnetic resonance imaging, requires the introduction of magnetic gradient coils. When an electric current is passed through these coils they produce a linearly increasing magnetic field B_1 along any of the three Cartesian axes (x,y,z) that sums up with the principal static field B_0. The resulting magnetic field B in the sample is therefore the vector sum of the main field B_0 and the field strength evoked by the imaging gradient B_1 and, therefore, B is a function of the spatial location. As the Larmor frequency of nuclear spins is a linear function of field strength, signals of different frequencies can be allocated to spatially differing areas in a volume resulting in spatially determined information. As a consequence, magnetic field gradients are used to define volumes of interest.

To encode the three dimensions of Cartesian space three different gradients are required. According to their role in the imaging process they are called frequency encoding, phase encoding and slice-selection gradients. For simplicity in the following description, these three gradients will be applied in x, y, and z-direction, respectively.

In most applications, the first step of image acquisition consists of selecting a slice within the volume by applying a gradient along the z-axis (G_z), i.e. along the magnet. This results in different precession frequencies according to their respective positions along the gradient axis. This allows for selectively exciting distinct slices by choosing the corresponding resonance frequency for the applied RF excitation pulse.

The thickness of the slice may be selected via the bandwith of the pulse.

$$z = \Delta\nu \,/\, \gamma G_s$$

where:
$\Delta\nu$ = frequency offset from ν_o (*i.e.* $\nu - \nu_o$)
G_s = magnitude of slice selection gradient
γ = gyromagnetic ratio

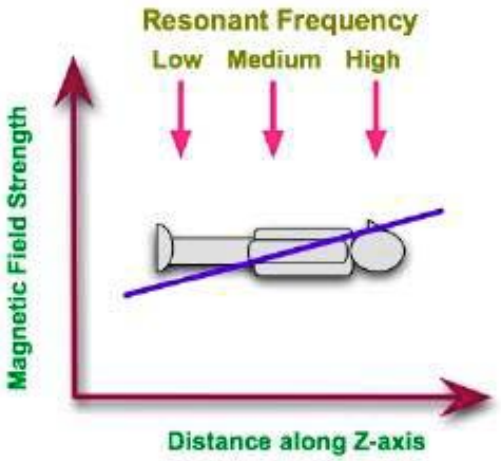

Figure 7. resonance frequency changes along a magnetic gradient and thus allows for selective excitation of a defined slice (reproduced from en.wikibooks.org/wiki/Image:ZGradient.jpg)

In order to assess spatial information within the selected slice a gradient perpendicular to the slice selection gradient, here in the y-direction, is applied. This changes the spins' precession frequencies and results in a phase difference between them according to the field strength they have encountered. According to the achieved effect this step is referred to as phase encoding.

To achieve full spatial encoding another gradient is applied, again usually perpendicular to the former two, in x- direction. This gradient, since it is switched on during data acquisition, is called read-out gradient or frequency encoding gradient. By this procedure an additional frequency encoding along the x-axis is achieved.

A two dimensional Fourier transformation is then applied to the recorded signal which results in an image of the selected slice. Spatial resolution is depending on the number of acquired data points and gradient switching schemes, as well as the thickness of the selected slice.

8.4.2 Functional magnetic resonance imaging (fMRI)

A functional imaging method of the central nervous system based on magnetic resonance was developed in the early 1990s (Ogawa, Lee et al. 1990; Kwong, Belliveau et al. 1992), referred to as functional magnetic resonance imaging (fMRI) neural activity is not observed directly as in EEG or MEG but rather via its metabolic consequences. This effect consists in localized changes in cerebral blood flow (rCBF), blood volume (rCBV) and oxygenation (BOLD) that accompany neural activity.

8.4.3 The BOLD effect

Blood consists of cellular and liquid components, the liquid being the blood plasma and the cellular component comprising thrombocytes, leukocytes and, as the major part, erythrocytes or red blood cells. These erythrocytes act as oxygen transporters from the lungs to all cells of the human body. Erythrocytes mainly consist of haemoglobin, an assembly of four globular subunits each of them being composed of a protein chain and a heme-molecule. The heme molecule, which causes the red colour of the blood, is built around a central iron atom which is the oxygen binding site of the molecule and makes deoxygenated haemoglobin paramagnetic. Once oxygen is bound to heme, the magnetic properties of the iron atom are attenuated, and the overall magnetic susceptibility is reduced, i.e. the heme molecule becomes diamagnetic. When deoxygenated, i.e. paramagnetic, erythrocytes show positive magnetic susceptibility and create a local magnetic field gradient to their diamagnetic surrounding that exhibits negative magnetic susceptibility. This local gradient

introduces a magnetic field inhomogeneity which results in decreased T_2* time and reduced MR signal at TE > 0 (see above).

When a certain region in the brain becomes active, local energy demand increases and so does oxygen consumption. This leads to an increase in regional blood perfusion (Villringer and Dirnagl 1999), accompanied by a subtle increase in oxygen extraction rate. This leads to the somehow paradoxical situation of a surplus of oxygen as a consequence of neuronal activity. Oxygenation on the arterial side of the resting brain is almost 100%, decreasing approximately linearly along the way through the capillaries down to about 60% on the venous side. Accordingly, the surplus of oxygenated blood during neuronal activity will cause an increase in blood oxygenation in the capillary bed and on the venous side of the vessel tree. Functional MRI techniques will, therefore, always depict changes in the capillaries and/or the draining veins of an active brain region. Following the principles described before this leads to less local dephasing and thus to a longer T_2* time in the region which is mirrored in a stronger image signal intensity in a T_2* weighted sequence. Accordingly, most of the sequences employed in fMRI are T_2* weighted and, reflecting the principle used to create them, are called blood oxygen level dependant (BOLD).

The change in the BOLD signal follows neuronal activity with a certain delay, usual in the order of several seconds. This delay varies region-specific which results from heterogenous vascular density in different regions as well as variable density of neurons and synapses.

8.4.4 Echo planar imaging (EPI)

Very fast measurement techniques are required to ensure the short image repetition times needed for adequate coverage of the hemodynamic response during stimulus presentation, especially for short tasks in event-related paradigms (e.g. face recognition, planning a movement or visual perception). Approaches that acquire all

image data after a single excitation pulse ("single-shot" techniques) are, therefore, the method of choice. Most often, echo-planar imaging (EPI) is applied, as it is readily available even on clinical scanners and does not require elaborate reconstruction procedures like spiral imaging sequences. Using EPI, acquisition times as short as 50-100ms per image are possible. EPI is a very demanding technique with respect to gradient performance, as the speed at which data points are acquired is primarily dependant on the gradient strength.

The idea of the EPI sequence concept was first proposed in 1977 by Nobel laureate Sir Peter Mansfield but its realization had to wait until appropriate gradient hardware became available in the 1990s. While conventional MRI samples each line of k-space after a separate excitation pulse, EPI achieves the acquisition of data to form a complete image within one single repetition time TR or one single "shot".

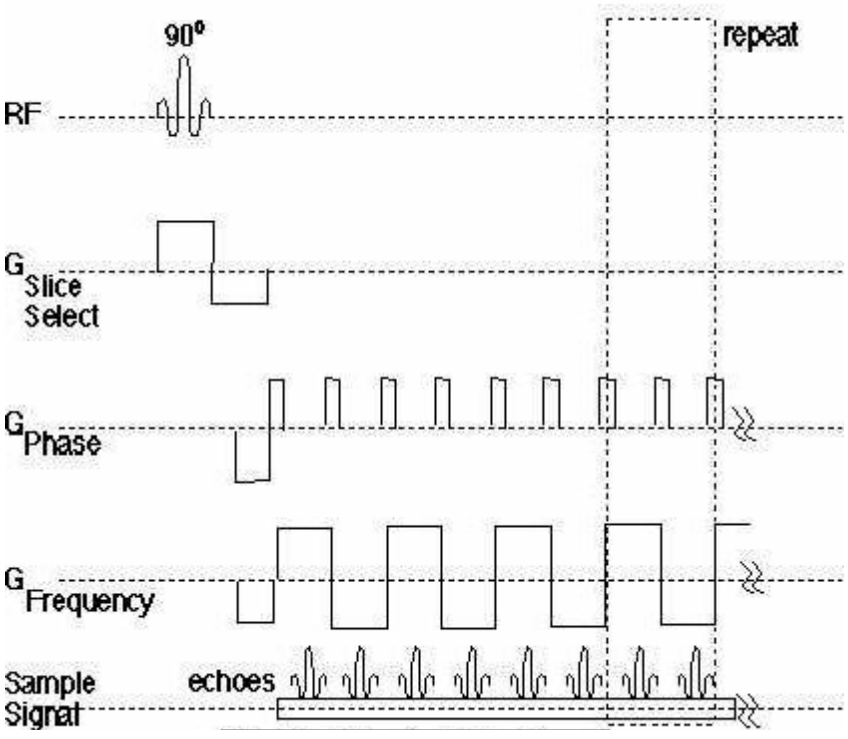

Figure 8. Echo-Planar Imaging (EPI) Sequence. Magnetization is focused to the slice-plane by the slice-selective RF pulse and is recalled multiple times by alternating frequency gradients $G_{frequency}$. All of the *k*-space is covered with a single excitation. Each individual echo is phase encoded by "blipping" G_{phase} prior to the collection data of each echo.

This results in an acquisition time around 40-100 ms for a 128 x 128 matrix compared to over 6 minutes using a conventional T_2-weighted imaging sequence. As mentioned above ultra fast imaging techniques like EPI have high requirements in terms of technical performance of scanner components, mainly concerning the gradient system. A combination of low-inductance gradient coils and high-performance amplifiers is required to ensure the high slew-rates necessary for ultra-fast imaging. Otherwise, rapid gradient switching will induce strong eddy-currents which are the primary cause of residual ghosting artefacts in EPI.

Rapidly changing magnetic fields may, however, also induce electrical currents in human tissue. Since these currents may lead to nerve stimulations, gradient performance limits have been imposed by EU and US legislation in order to protect patients.

Acoustic noise is also a point of considerable importance for fMRI, especially if acoustic stimuli are part of the experimental paradigm. This noise is a consequence of the rapid switching of gradients and is caused by small movements of the gradient coils propagated by the tube-like structure of the magnet.

8.4.5 fMRI Studies

The signal changes in BOLD-sensitive sequences caused by neuronal activity are around 1-5% at 3 Tesla, i.e. in the order of the signal to noise ratio (SNR). In model-based analysis approaches the functional data (time series) acquired during stimulus presentation or task performance is compared with data from acquired during an assumed resting state to obtain information about functional activation in the brain. Differences in BOLD signal intensities undergo statistical testing to obtain maps of significant BOLD- activation.

Careful selection and design of stimuli to be perceived or tasks to be performed by the subject during the scan are crucial to the conclusions to be drawn from the observed data. In an fMRI experiment there are two principal modes of presenting a stimulus paradigm.

In **block design** paradigms stimuli are presented continuously for a fixed period of (typically) tens of seconds and are alternated by a baseline condition of equal length. This procedure is generally repeated several times to improve sensitivity.

In **event-related designs** a stimulus is presented for short periods only. If the subject is required to respond to a given stimulus (e.g. choosing between a yes- and a no button) then this response will typically trigger progression to the next baseline or stimulus condition. This way specificity is improved at the cost of sensitivity. A variety of test paradigms including cognitive and motor tasks are realized this way.

8.5 Surface based Analysis of structural MRI data

8.5.1 Introduction

With the availability of functional imaging techniques and the resulting production of very large data sets containing activation data with high spatial resolution, data visualization and analysis have arisen as challenging tasks. The key issue is to reduce the amount of data while preserving information about spatial and topological relationships of functional areas. This was of prime interest for the current study.

Adequate post-processing of functional maps is crucial for the assessment of retinotopy in the human cortex. The procedures described in the following paragraphs aim at presenting functional visual areas in the human cortex in a way that allows statistical analysis to test the hypotheses to be performed (chapter 7). The human cerebral cortex is extensively folded exhibiting its characteristic topology of gyri and sulci. Consequently, the total surface area of about 1800 cm² largely extends

the area of its containing structures, the meninges and the skull. In a conventional native 3-dimensional volumetric display the true extent of the cortical surface area can hardly be assessed correctly. Stereotaxic parameterization such as the one by Talairach & Tournoux (Talairach and Tournoux 1988) will not - in general - reflect the correct neighbourhood relationships between distinct cortical areas and is thus unsuitable for the evaluation of experimental data that varies as a function of its position along the cortical surface, such as the one described in this study.

It has been argued that the most favourable way to visualize the cortex, due to the average cortical thickness of only about 3-5 mm, is to treat it as a two dimensional sheet-like structure (Van Essen, Drury et al. 1998). Since the BOLD- signal in functional magnetic resonance imaging mainly originates in the grey matter of the cortex the visualization of underlying white matter can be ignored when assessing the distribution of functional areas via fMRI. Compared to classical approaches the surface based method yields the advantage of treating the cortex as a connected structure, an aspect neglected in the slice wise display of volumetric data. Visibility of cortical areas hidden in the depths of sulci can be enhanced by smoothing and inflating the surface model to an ellipsoidal structure which, at the cost of some discontinuities and geometrical distortions, can be morphed to a flat, two dimensional maps. Onto Functional data can be projected onto such flattened representations employing various algorithms. Due to the 2-dimensional Cartesian parameterization of a flat surface it is well accessible to statistical parametric analysis.

	Native 3D	Slices	Smoothed Surface model	Flat map
Visibility	Poor	Interval dependent	Good	Excellent
Surface topology	Good	Many cuts	good	Some cuts
Compactness	Moderate	Poor	Moderate	Excellent
Foreshortening	Poor	Axis dependent	Poor	good
Distortions	Low	Low	Moderate	Moderate
Parameterization	Stereotaxic (3-D)	Stereotaxic (3-D)	None	Surface-based (2-D Cartesian)
Ease of localization	-	Mixed	Good	mixed

Table 5. Comparison of visualization approaches. Evaluation is done with respect to visibility of buried cortex, topology (cuts in the surface), compactness (number of needed views), geometrical distortions, additional perspective distortions, coordinate systems available for parametrization and the ease of localization relative to the native 3-D configuration. Adapted and modified from (Van Essen, Drury et al. 1998)

8.5.2 Segmentation

The first step for isolating the cortical surface out of brick of voxel-data is to assign voxels to different tissue types. A completely manual approach would be to draw the borders of neighbouring tissue types directly onto the raw image. Since this would be an extremely time- consuming procedure automatic tissue classification algorithms have been developed (an overview of current algorithms is given in (Tosun, Rettmann et al. 2004)). This so-called tissue segmentation relies on the MR image contrast between cortical grey matter, white matter and cerebrospinal fluid in T_1-weighted images. As a prerequisite for adequate tissue segmentation, MR data sets must be acquired with high spatial resolution imaging and good SNR (signal to nosie ratio) and CNR (contrast to noise ratio).

The first step in segmentation usually involves manual or automatic definition of the ranges of signal-intensities for distinct tissue classes. For several reasons valid tissue classification can not rely solely on this first step. Most importantly, the distributions

of brain grey and white matter voxel intensities can overlap considerably, thus producing ambiguous results in an exclusively intensity based segmentation approach. Furthermore, not all anatomical boundaries in the brain coincide with intensity-based limits, e.g. the boundary between left and right hemisphere at the corpus callosum show no intensity difference at all.

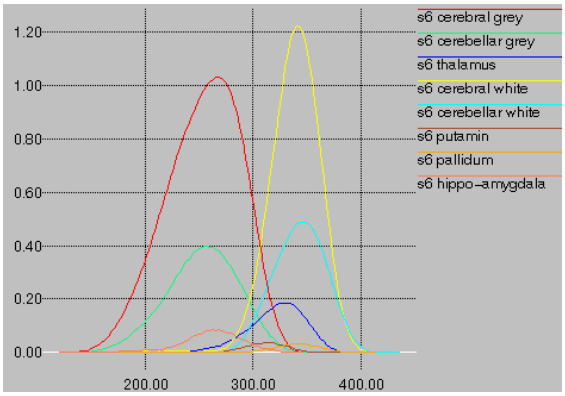

Figure 9 signal intensity distribution in distinct brain areas, (reproduced from http://www.cma.mgh.harvard.edu/seg/auto_f/prob_f/overlapping_intensities.html)

Partial volume effects occur when a voxel reflects more than one tissue class. Consequently, intensity discrimination is blurred by signals originating from different tissues. Boundaries between cerebrum and cerebellum or between both hemispheres are prone to such effects since adjacent tissues often exhibit similar grey scale values. Usually bias arises in MRI from magnetic field inhomogeneities during the scanning process. This results in smooth intensity variation within the volume. Such intensity gradients along a volume resulting from RF-field inhomogeneities, while usually not being a problem for visual inspection by a radiologist, may render automated segmentation, which relies on similar ranges of intensity for one tissue class in an anatomical volume, futile. Therefore, this needs to be corrected during the pre-processing of structural data. A simple, yet effective approach for correction of this RF-bias can be achieved by dividing the volume by an extensively smoothed version of the same data set, removing low spatial frequency intensity changes while preserving high spatial frequency structural information. Inhomogeneity correction

in the current study was achieved by utilization of an extended mixture of Gaussians model (MOG), a standard technique employed by several tissue classification algorithms and the additional use of tissue probability maps (Ashburner and Friston 2005).

As described above, structural data sets may be contaminated by various artefacts that render simple tissue segmentation approaches useless. Suitable tissue segmentation techniques therefore employ sophisticated algorithms and prior assumptions to accomplish their goal. The SureFit-Algorithm used in this study relies on a manual definition of grey- and white matter peaks. Besides intensity based estimation edge detection employing intensity gradient calculation as well as prior knowledge about plausible cortical shapes is included in the process of demarcating the cortical surface. For a detailed description see (Van Essen, Drury et al. 2001). Large blood vessels, noise and other inhomogeneities cause topological errors in the segmentation result. In the surface reconstruction, these errors appear as bridges of grey matter between neighbouring gyri (exohandle) or holes through a gyrus from one sulcus to the next (endohandle). Automatic correction of these artefacts is a very time-consuming procedure and far from perfect in removing all defects, thus manual inspection and editing of the segmentation volume is still necessary. This problem is intensified in subjects with pathologies resulting in altered brain structure, such as neoplasms, cysts or altered gyration due to genetic disorders.

Figure 10 provides a schematic description of the workflow used in this study illustrated by intermediate results and screenshots obtained from the software employed. As mentioned above, high resolution image data with high quality in respect to signal to noise ratio and homogeneity of intensity within tissue classes are required for successful segmentation. Details of the sequence optimized for use at high field (3 Tesla) employed to meet these prerequisites are presented in chapter 9.4.2

Surface extraction workflow

1. Preprocessing →High quality T_1 weighted homogeneous MR-Image

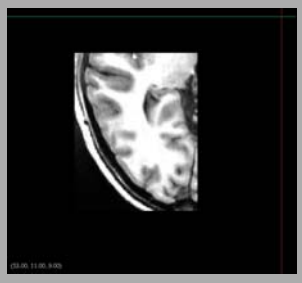

2. Manual definition of intensity peaks of different tissue classes

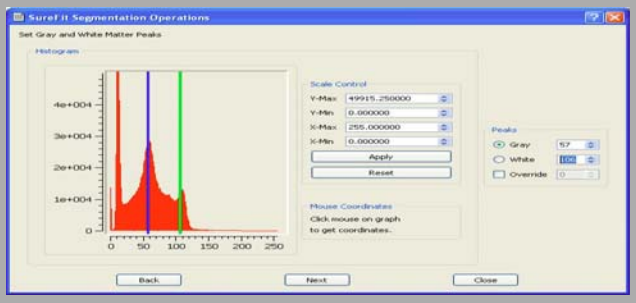

3. SureFit algorithm → Segmentation volume

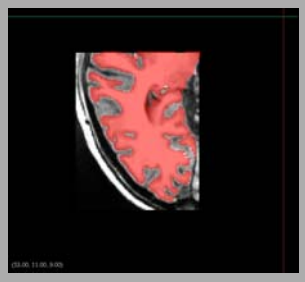

4. CARET → Mesh-model of cortical surface

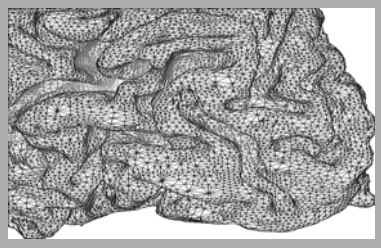

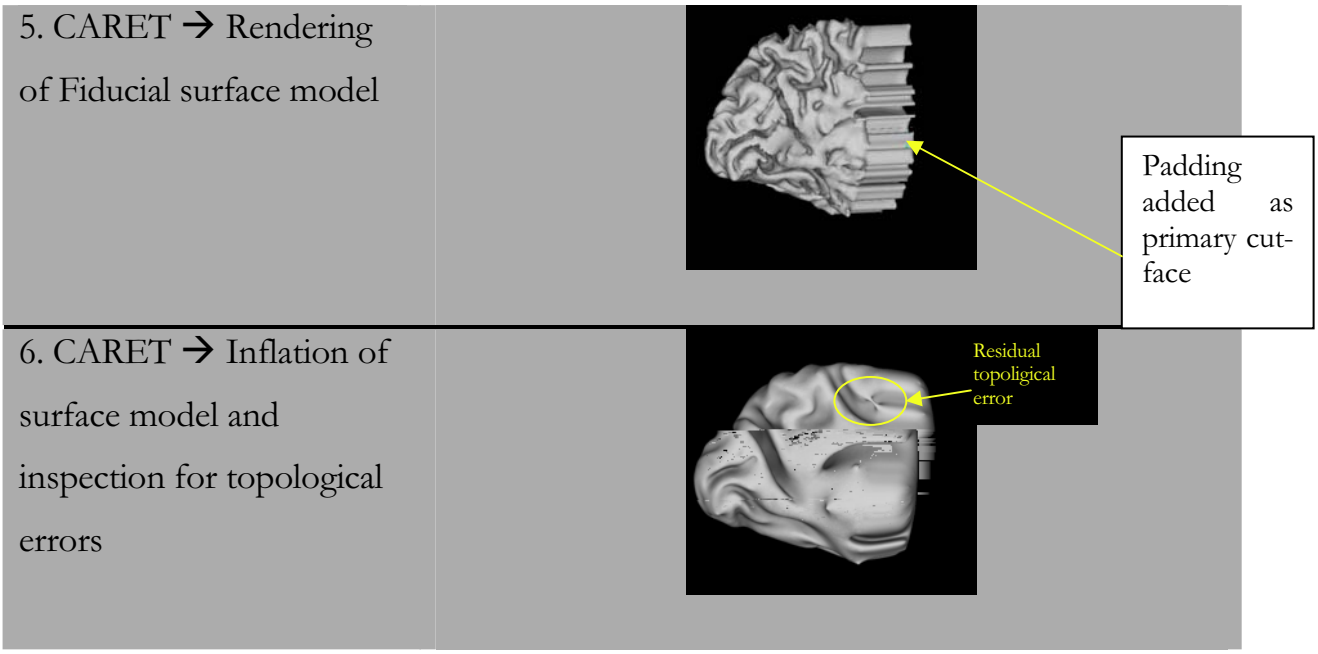

Figure 10. Illustration of the steps to be performed for cortical surface reconstruction. Only the occipital lobe as region is processed here. To achieve a closed topology a padding is added to the frontal face of the partial hemisphere. This padded area later serves as cut-face when creating a flatmap

8.5.3 Surface generation and flattening

Once satisfactory segmentation is achieved, a mesh-model of the surface can be generated. Applying suitable algorithms that mesh-model can be inflated to reveal structures buried in the sulcal depth. To generate a flattened 2D representation the closed topological entity needs to be cut. Once cuts have been applied to the inflated model, residual geometric distortions can be minimized by so-called iterative morphing (Drury, Van Essen et al. 1996). Structural information about sulcal depth and folding implicitly present in a volumetric visualization is not lost in surface-based analysis of anatomical MRI volumes; rather it is explicitly quantified and assigned to each node on the surface. Remaining geometrical distortions of flattened cortical maps are also assigned to each node. While the former makes the anatomical brain structure itself accessible to statistical investigation, e.g. in (Van Essen, Dierker et al. 2006), the latter allows for corrections when performing statistics on flat maps. Figure 11 - Figure 13 show examples of structural information inherent to

volumetric data or resulting from surface deformation made available for analysis via surface based analysis

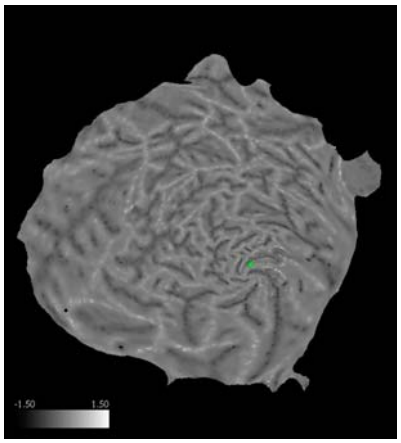

Figure 11. Cortical folding visualized as grey values on flattened occipital lobe representation

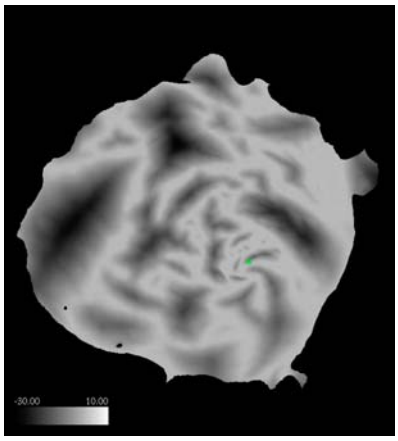

Figure 12. Cortical depth visualized as grey values on flattened occipital lobe representation

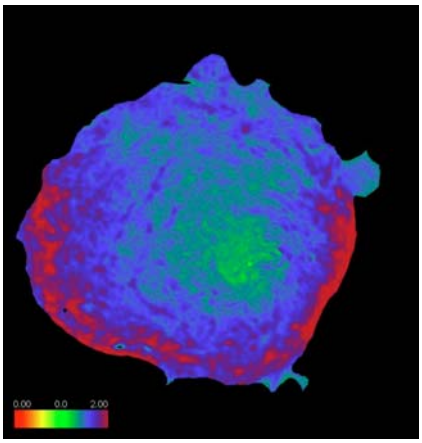

Figure 13. Colour-coded distortion map of flattened occipital lobe

9 Methods

9.1 Subjects

Multimodal Imaging including PET, structural and functional MRI was performed in 7 healthy subjects (6 females, 1 male), aged 24.4 ± 2.2 years (mean ± SD)

fMRI data were measured in the project "**A multimodal study combining fMRI and PET to investigate serotonergic modulation of limbic excitability in patients with anxiety disorders**" (principal investigator: Rupert Lanzenberger, MD) funded by the Austrian National Bank (OENB P11468).

Quantitative serotonin-$_{1A}$ receptor data have been acquired in the PET study "***In vivo* imaging of** 5-HT$_{1A}$ **receptors using PET in patients with anxiety disorders and healthy controls**" funded by the Austrian Science Fund (FWF P16549) as published in Lanzenberger et al. 2007

9.2 Radiochemistry

The radiotracer [*carbonyl*-^{11}C]WAY-100635 was synthesized at the Cyclotron Unit of the PET centre at the Department of Nuclear Medicine, Medical University of Vienna, Austria. The synthesis procedure described previously by Mattarese (Matarrese, Sudati et al. 2002) was slightly modified (Wadsak 2007) and carried out in a fully automated PET synthesizer (GE Healthcare, Uppsala, Sweden). Further details can be found in Lanzenberger et al. 2007 and Wadsak et al. 2007.

9.3 PET Scanning Protocol and Preprocessing

9.3.1 Data acquisition

The PET data sets were acquired on a GE Advance PET scanner (General Electric Medical Systems, Milwaukee, Wisconsin) at the Department of Nuclear Medicine, Medical University of Vienna, Austria.

Subject heads were aligned in the scanner parallel to the orbitomeatal line by means of a laser beam system. In order to avoid gross head movements, patients were fixated with straps around forehead and chin as well as with a polyurethane moulded pillow. Communication with the operating personnel was achieved via hand signals, as all study participants were instructed not to speak during the scanning procedure.

For correction of tissue attenuation a 5-minute transmission scan was performed in two-dimensional mode using a retractable ^{68}Ge ring source.

Acquisition of dynamic PET scans was done in 3D-mode commencing simultaneously with intravenous bolus injection of the radioligand [*carbonyl*-^{11}C]WAY-100635 in phosphate-buffered saline. An average dose of 5.86 ± 0.55 MBq per kilogram body weight was administered. 30 consecutive time frames (15 * 1 minute, 15 * 5 minutes) were acquired, leading to a total measurement time of 90 minutes.

9.3.2 PET preprocessing and image reconstruction

Based on the transmission scan results scattering and tissue attenuation in the emission data were corrected for. An iterative filtered back-projection algorithm (FORE-ITER) was used for reconstruction of 35 contiguous slices (matrix 128 *128) with a thickness of 4.25 mm each. Spatial resolution of the reconstructed volume was 4.36 mm full-width at half maximum (FWHM) at the centre of the FOV. Partial volume correction or realignment for head movements was not performed. All 30

dynamic PET frames were summed up (PET_{ADD}) for co-registering of PET data sets to the structural MR image, which was done with SPM5 (http://www.fil.ion.ucl.ac.uk/spm/).

9.3.3 Estimation of the 5-HT$_{1A}$ receptor distribution using kinetic modelling

Receptor distribution estimation was done with the PMOD 2.6 software (http://www.pmod.com/). Kinetic modelling was based on the simplified reference tissue model (Lammertsma and Hume 1996) with the cerebellum as reference region. Figure 14 depicts a resulting 5-HT_{1A} receptor binding potential map overlaid on a surface 3D model of coregistered structural MR data in a single subject. This view clearly illustrates low receptor distributions in primary sensory areas such as the visual area located at the occipital pole and the primary somatosensory and motor area at the central region.

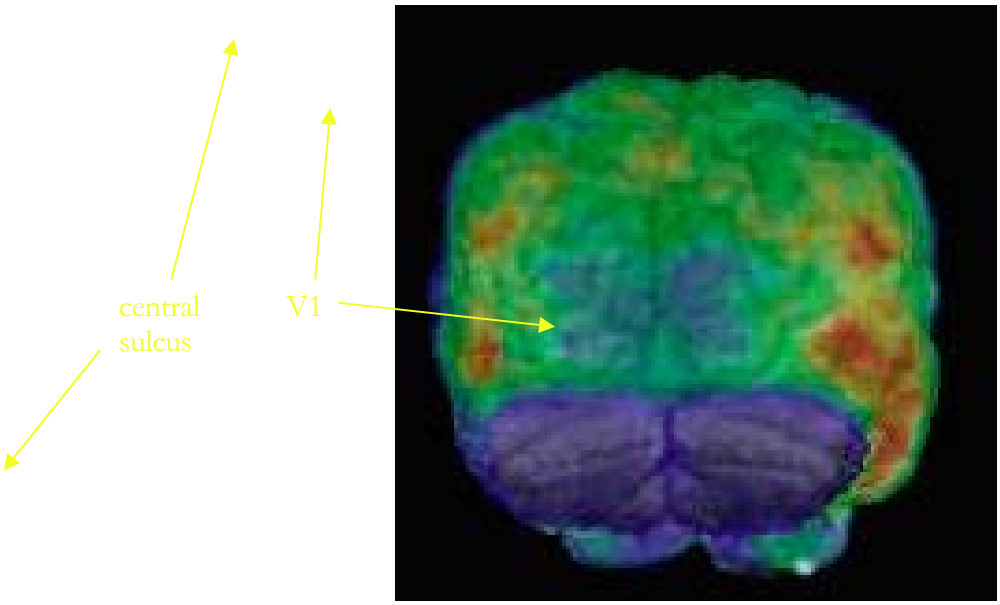

Figure 14. 5-HT_{1A} receptor distribution map. The underlay is a coregistered anatomical MRI scan from the same subject

9.4 Functional magnetic resonance imaging (FMRI)

The challenges in the study at hand were:

1. To create flattened representations of the visual cortex.
2. To generate retinotopic maps defining different visual areas.
3. To overlay retinotopic and neurochemical maps on the flattened cortex.
4. To assign borders of functionally defined visual areas using data acquired during the retinotopic paradigms in order to perform further comparisons according to the working hypotheses of this thesis.

9.4.1 Preparations for MRI- scanning procedures

During both structural and functional scans patients were fixated in the head coil using wedge-shaped cushions and straps around the forehead to minimize head movements. Study participants were also instructed not to move. Communication with the subjects between separate scanning runs was established via a headset and microphone. For cases of urgency during the scanning procedure patients held an emergency button device in their left hand, which, once activated rang an alarm in the supervision room. During preparation scans before and during anatomical imaging at the end of the functional runs, subjects were encouraged to relax with a video display and soft music to reduce stress for improved compliance and enhanced comfort during the experiments.

9.4.2 Anatomical magnetic resonance imaging (MRI measurements)

High-resolution T_1-weighted structural MR images (MPRAGE sequence, 256*256 matrix, 0.78*0.86mm voxel size, slice thickness 1.56mm, 128 slices) were acquired in a 3 Tesla Medspec whole-body MR scanner (Bruker BioSpin, Ettlingen, Germany) using the standard birdcage headcoil.

Figure 15. The 3 Tesla BRUKER Medspec 30/100 scanner at the Vienna MR centre of excellence was used for both anatomical and functional imaging in this study

9.4.3 Preprocessing of structural data

The structural data were imported from the proprietary scanner format and converted to SPM/Analyze format. Further preprocessing steps were performed in SPM5 (http://www.fil.ion.ucl.ac.uk/spm/software/spm5).

In a first step the anatomical volume was normalized to standard space defined by the Montreal Neurological Institute (ICBM, NIH P-20 project) approximating the atlas of Talairach and Tournoux (Talairach and Tournoux 1988). The procedure referred to as normalization involves a nonlinear deformation process, where the volume in focus is adjusted to comply with a standardized template image. This step

is usually required for voxel-wise statistical testing across a subject group. In our case it was used in preparation for the segmentation process and to enable automatic script based manipulation of multiple volumes.

In a subsequent step the volume underwent a bias field correction. The procedures employed by SPM5 to perform bias correction are described in (Ashburner and Friston 2005).

Structural data needed to be separated into right and left hemisphere volumes in order to enable surface-reconstruction within the CARET software package. Little manual adjustments were required, as the preceding spatial normalization in general yielded optimal results. Structural data set size was reduced by cropping anterior parts of the brain, leaving only the region to be analyzed, namely the occipital lobe.

9.4.3.1 Segmentation of structural data

Segmentation of the structural images and building and flattening a cortical surface model out of segmentation data was done with the CARET software suite 5.5 (Van Essen, Drury et al. 2001). While a lot of preparation work could be implemented in an automated work stream realized with the bash scripting language under Linux several steps required manual intervention. Those steps included adjustments to the intensity scaling of the images, initial definition of grey- and white matter peaks as well as correction of residual segmentation errors.

9.4.3.2 Construction and flattening of the cortical surface model

A mesh-model of the surface was constructed based on the segmented volume. Inflated versions also created from this initial surface model were used for visual inspection for topological errors. Since the data sets comprised the occipital part of the brain only, the requirements for open topology were already fulfilled and opening of sulci in order to reduce distortions was thus not required. Additional cuts were, however, applied to reduce the flattened surface to the area where functional data was available and to remove residual topological errors at the edge of the map.

9.4.4 Functional MRI of the visual cortex employing retinotopic paradigms

9.4.4.1 Stimuli used in the retinotopic paradigm

Retinotopic stimuli used in this study were based on previously published studies (Engel, Glover et al. 1997; Tootell, Hadjikhani et al. 1998; Warnking, Dojat et al. 2002; Dumoulin, Hoge et al. 2003). Programming of the stimuli was done using home-written software using the Interactive Data Language, IDL (ITT visual Information Solutions). The experimental design involved the presentation of two opposing checkerboard-wedges, each about an eight of the display in size in a "propeller" configuration that reversed contrast polarity at 8 Hz and rotated clockwise around a fixation cross at a rate of 1 cycle per 64 seconds. The purpose of this stimulus was to create a traveling wave of activation in the areas associated with different angels of polarity in the visual field. Since the upper and lower vertical meridian are represented at opposing borders of V1, which are in the same axis as the calcarine sulcus, the activation wave travels from border to border and is used to identify the borders of V1 to V2.

A second stimulus, a checkerboard ring with the same reversing rate that expanded from the fixation to the periphery of the visual field at a frequency of two per minute was presented. This stimulus, first used by (Engel, Rumelhart et al. 1994) was used to create periodic activation in the areas of the visual cortex associated with different angles of eccentricity the field of view. The speed of expansion of the ring increased linearly with its diameter. This was done with respect to the cortical magnification factor (Engel, Rumelhart et al. 1994; Tootell, Hadjikhani et al. 1998) in order to evoke a BOLD-response wave traveling at constant speed. Since eccentricity mapping does not provide any information about functional borders, the data acquired from this paradigm was not included in further analysis.

9.4.4.2 Presentation

Stimuli were projected from outside of the scanner room via a mirror to a screen positioned in the head-side gantry of the MR scanner using a video beamer (SANYO, Japan). Study participants watched the stimuli via a small mirror mounted on the head coil. This mirror was adjusted to allow comfortable viewing over longer periods. Stimulus timing was controlled with the Presentation software (Neurobehavioural Systems Inc., Albany CA). Stimulus presentation was initiated simultaneously with the start of fMRI data acquisition. Subjects were instructed to fixate the middle of the screen and asked to maintain fixation during the whole stimulus presentation. The fixation point was marked with a white cross during blank periods. This layout produced a stimulation of approximately the central 30° of the visual field in both directions.

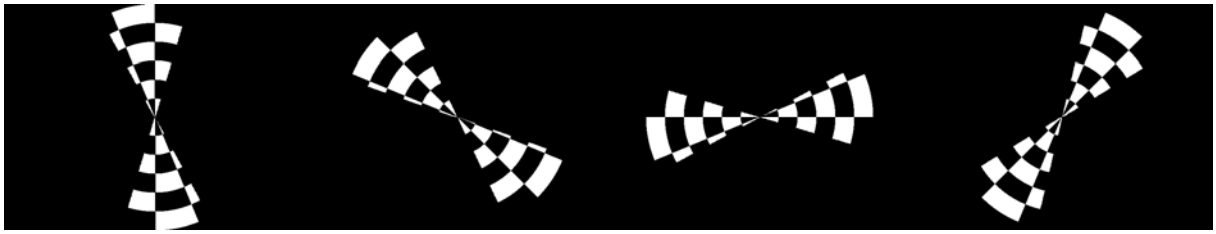

Figure 16. Rotating wedge paradigm

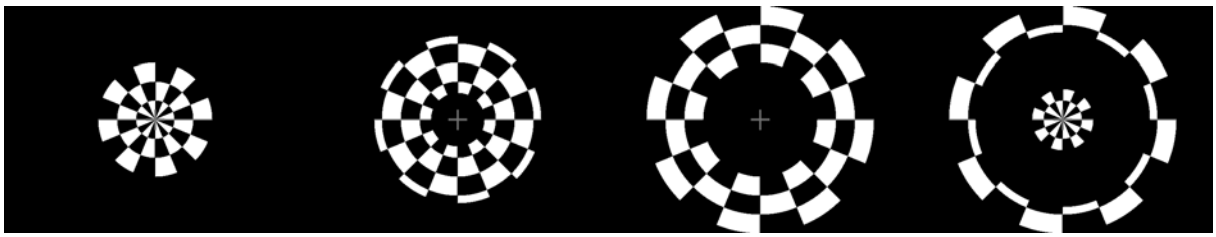

Figure 17. Expanding ring paradigm

Each of the two stimuli was presented for 4 cycles resulting in a measurement time of approximately 2 minutes per run. Stimulus presentation was preceded with a 10s dummy scan period which was required to ensure steady-state magnetization conditions.

9.4.4.3 fMRI data acquisition

Functional imaging was performed in a 3 Tesla Medspec whole-body MR scanner using high resolution gradient-recalled echo planar imaging (EPI). Ten oblique axial slices centered on the calcarine sulcus were acquired using asymmetric k-space sampling (matrix size 128 x 91, slice thickness 2 mm, slice gap 0.5 mm, TR = 1000 ms, TE = 31 ms). During each functional session a high resolution whole brain EPI-Image was acquired for later normalization purposes.

9.4.4.4 Preprocessing of functional data

Functional volumes were reconstructed from raw k-space data and were converted to Analyze-format for further processing in SPM5. Data sets underwent correction for slice timing, as well as motion correction through rigid body registration of each timeframe to a mean image. Inspection of correction parameters exhibited high quality data for all data sets. The whole-brain EPI volume was normalized to a template in MNI-Space and the resulting deformation matrix was applied to each of the functional volumes. Functional data was acquired at three to four different sessions and were thus oriented differently due to varying positioning of the patient in the scanner. This problem was accounted for by adding up the data sets after normalization and dividing the result by a mask based on individual brain coverage. The resulting weighted average volumes were smoothed with a Gaussian kernel (6mm FWHM) to further increase SNR and then used for further analysis.

9.4.4.5 Analysis of phase-encoded data

Volumetric analysis of phase-encoded data including signal-to-noise estimation was performed with home-written software in Interactive Data Language. For analysis purposes each 128 successive time frames were imported into a single 4-dimensional data array. The resulting array contained a time series of the intensity of each voxel in standardized MNI space (79 x 95 x 69 x 128). Each voxel time series underwent fast Fourier transformation for frequency spectrum analysis. Due to the experimental design each visual hemifield was stimulated 4 times by a wedge of the rotating

propeller during the 128 seconds of measurement. Thus, the stimulation frequency ν_0 to be examined in the time series was four.

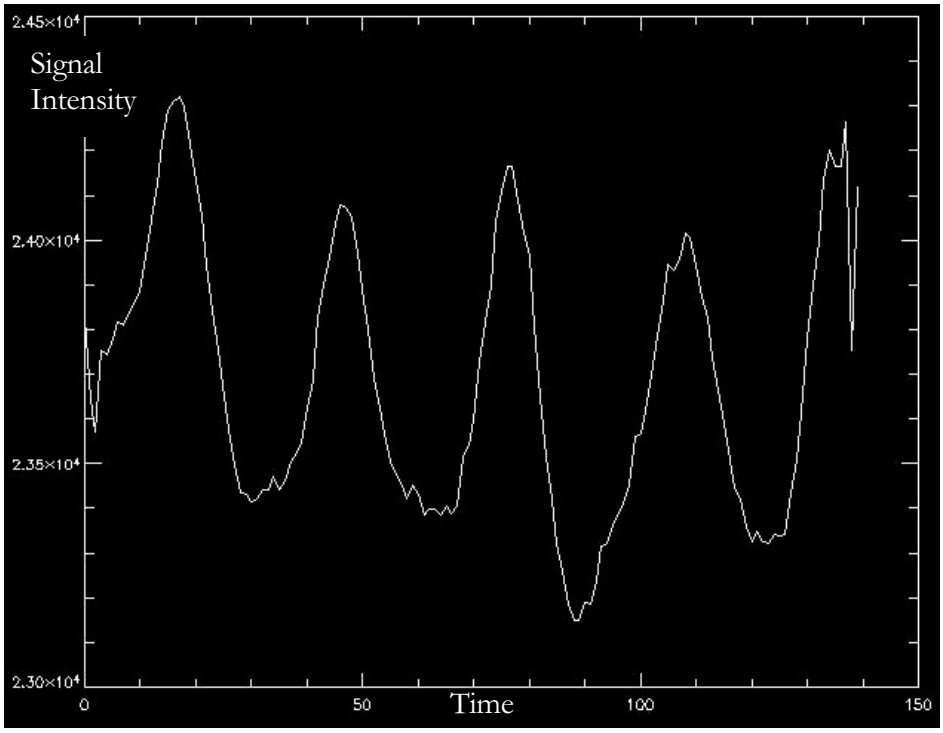

Figure 18. Intensity-Time course (150 frames, boxcar smooth of 7 averages) of a voxel in the visual cortex during the paradigm.

The actually measured phase φ and amplitude A of the response at the stimulation frequency ν_0 are

$$\varphi_j = \arg(F_{v0}(\vec{X}_j))$$

$$A_j = \left| F_{v0}(\vec{X}_j) \right|$$

SNR was estimated in each voxel in order to assess the reliability of the calculated phase φ. This was done following the approach described by (Warnking, Dojat et al. 2002). Since the noise at stimulation frequency is not directly accessible it was approximated based on the assumption that frequencies above stimulation frequency ν_0 contain only noise, while those below ν_0 may include baseline drifts and were

therefore excluded from the estimation process. Noise level was calculated for each voxel as the standard deviation of the real and imaginary spectra across all frequencies above ν_0. All harmonics of ν_0 were excluded from this calculation. The ratio between response amplitude (A) at stimulation frequency and estimated noise (σ) provided a measure of the SNR value for each voxel.

$$SNR_j = \frac{A_{v0}}{\sigma_{v0}}$$

Figure 19 exemplifies the results of the volumetric analysis of phase encoded retinotopic stimulus. Ten slices obtained by performing the analysis procedures described on one 4-dimensional time series registered by employing the abovementioned technique of echoplanar imaging are presented. The upper two rows show the amplitude of the BOLD-signal change at stimulation frequency, while the middle two rows depict the according phase information encoded as grayscale values, ranging from –π (black) to +π (white). By applying the portrayed SNR estimation approach described above, as shown in the lower two rows, the occipital cortex can easily be singled out as the prime area affected by the employment of the visual stimulus used. The effectiveness of the method can visually be judged by comparing the amplitude display in the top rows with their corresponding SNR-weighted slices

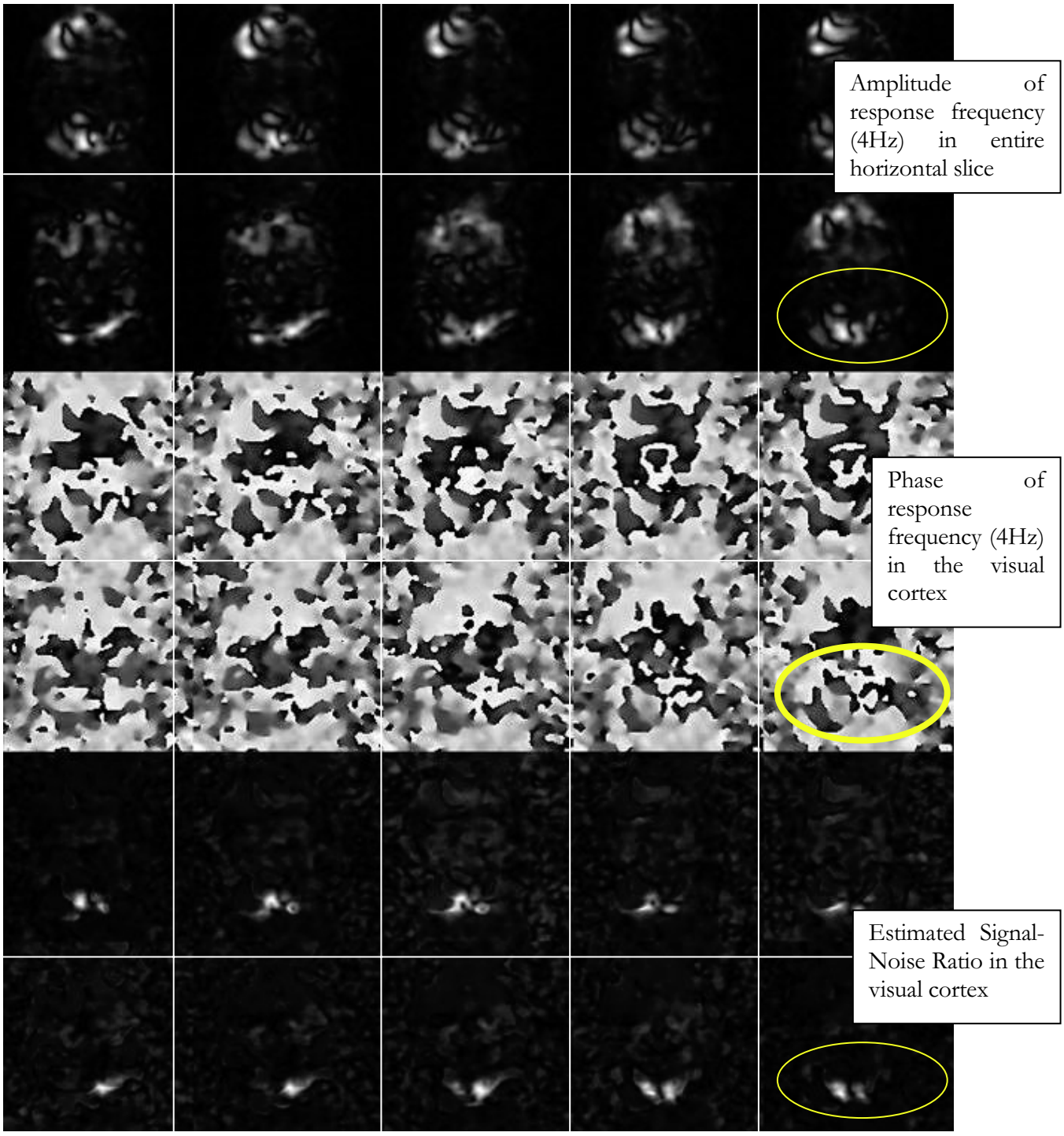

Figure 19 Given are signal amplitude, phase and signal/noise ratio for 10 horizontal slices at height of the visual cortex. The encircled areas indicate the position of the occipital lobe, where the visual cortex is located.

9.4.4.6 Assignment of retinotopic phase maps to the cortical surface model

Estimating the location of a cortical response on a reconstructed surface based on volumetric data requires assumptions about the contribution of each voxel to each node of the cortical mesh-model to be made. Several mechanisms may lead to a mismatch between cortical response at the location of a given node and 3-dimensional data acquired at or close to that node. Partial volume effects in voxels that include both grey matter and tissue not exhibiting functional response, as well as several physiologic artifacts (circulation, respiration, head movement) introduce noise into the measurement leading to a misestimation of phase in the respective voxel. Accordingly, voxels with SNR below 2 were excluded from assignment to the cortical surface to reduce phase estimation errors. Another issue to consider is the case of neighboring banks within a sulcus, particularly in the calcarine sulcus where voxels with high SNR at stimulation frequency may exhibit completely different phases due to their true distance along the cortical surface resulting in phase errors up to +-90°. Following the considerations discussed in (Warnking, Dojat et al. 2002) the "enclosing voxel" algorithm, attributing data to the node closest to the respective voxel, was used for mapping phase and SNR data to the surface model.

9.4.4.7 Delineation of visual areas on the cortical surface model

An automatic method for delineating visual area borders based on eccentricity as well as polarity mapping experiments has been proposed by (Sereno, Dale et al. 1995). Although this approach has been implemented within the current project, it was found unreliable and delivered suboptimal results; therefore, a manual delineation approach was chosen for this study. Due to the experimental design that produces a standing wave of activation from the upper border to the lower or vice versa, depending on stimulus orientation, visual borders are expected where the phase mapping reaches a local maximum (+π) or minimum (-π). These regions were visually identified and the border was drawn along these local maxima or minima. This procedure of identifying visual areas based on retinotopic data applied here was

summarized by H. Baseler (http://white.stanford.edu/~sweta/VistaLab/Manual/retinotopy.html). Since the border region between primary and secondary visual areas rather than the whole extent of visual areas was of interest in this investigation delineation was limited to those areas where fMRI data has been acquired.

9.4.4.8 Assignment of neurochemical data to the cortical surface model

Quantitative serotonin$_{1A}$ receptor data was assigned to the surface employing multiple mapping algorithms;

1. In order consider the whole cortical thickness at a specific point in the surface model the maximum value in a 4 x 4 x 4 mm box around this node was assigned.

2. In the "nearest neighbor" approach, the functional value of the voxel located closest the stereotactic position of a node in the fiducial mesh model was assigned to this respective node.

3. A Gaussian weighting kernel with 4 mm FWHM normal and tangential to the surface was used to include data around a certain node. Data from above the surface were, however, considered only within a cutoff-distance of 1 mm.

4. The average binding potential data within a 4 mm box surrounding the stereotactic position of a surface node was assigned to this node.

This way, four different mappings were acquired for further comparison.

9.4.4.9 Regions of interest (ROIs)

Regions of interest were circumscribed with CARET on both sides of the retinotopically defined V1/V2 border. Size of ROIs was chosen to be comparable in individual hemispheres. An additional ROI aimed at enclosing delineated primary visual cortex area was defined between the dorsal and ventral V1 borders.

Manual delineation was done according to the principles described in section 9.4.4.7 gives a typical example of a set of delineated regions of interest. An inflated representation of the occipital lobe accompanies the flat map to increase visibility. The black lines indicate the retinotopically defined ventral and dorsal V1/V2 border while the light blue lines circumscribe ventral and dorsal V1 ROIs. Likewise, red lines demarcate V2 ROIs. The green spotted area indicates the whole V1 region of interest used as an additional source for comparison.

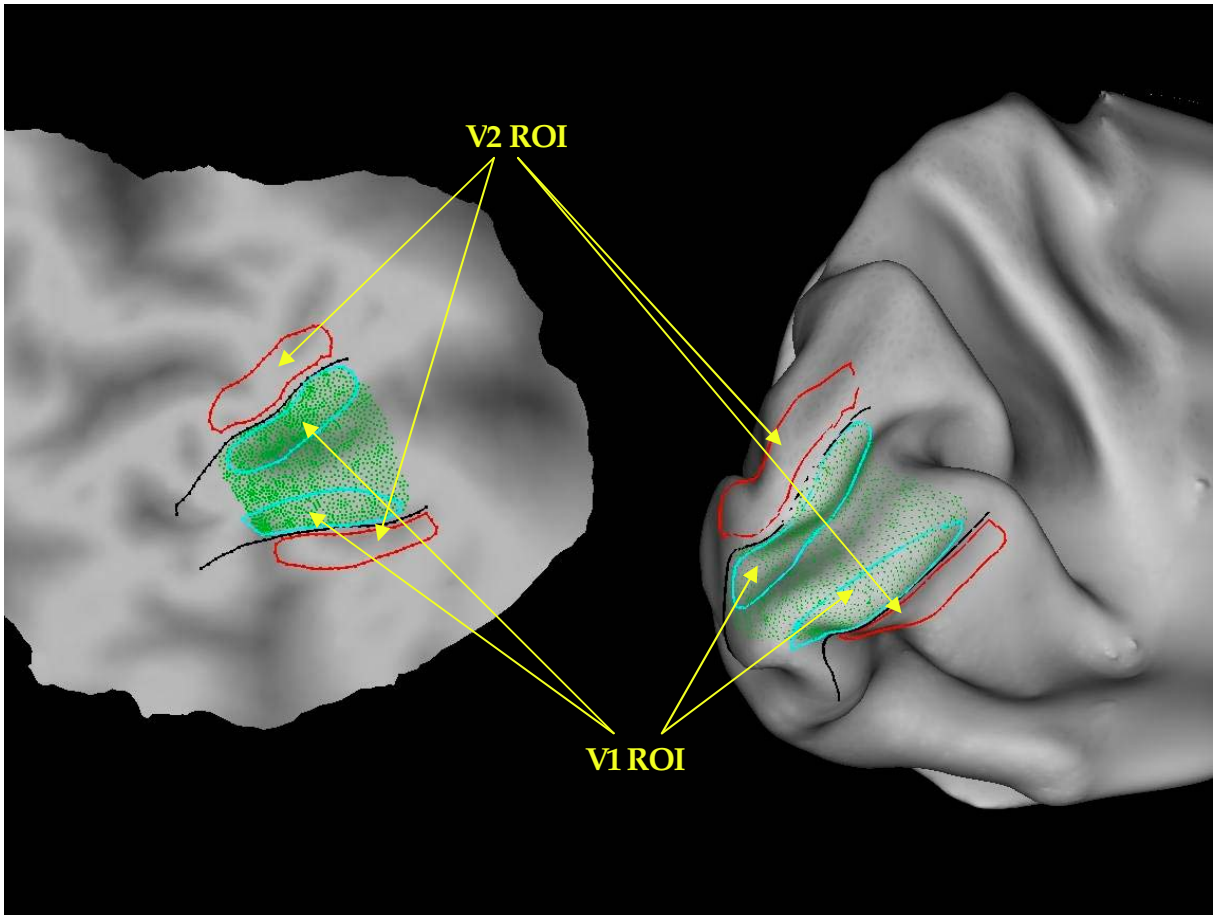

Figure 20. Flatmap and inflated surface model showing ROIs for V1 (light blue), V2 (red) and whole V1 (spotted green area)

The resulting mappings of both fMRI and PET data to the various surface models reconstructed from the anatomical MR volume are exemplified in Figure 21. The projected functional borders and delineated ROIs were defined following the procedures described above.

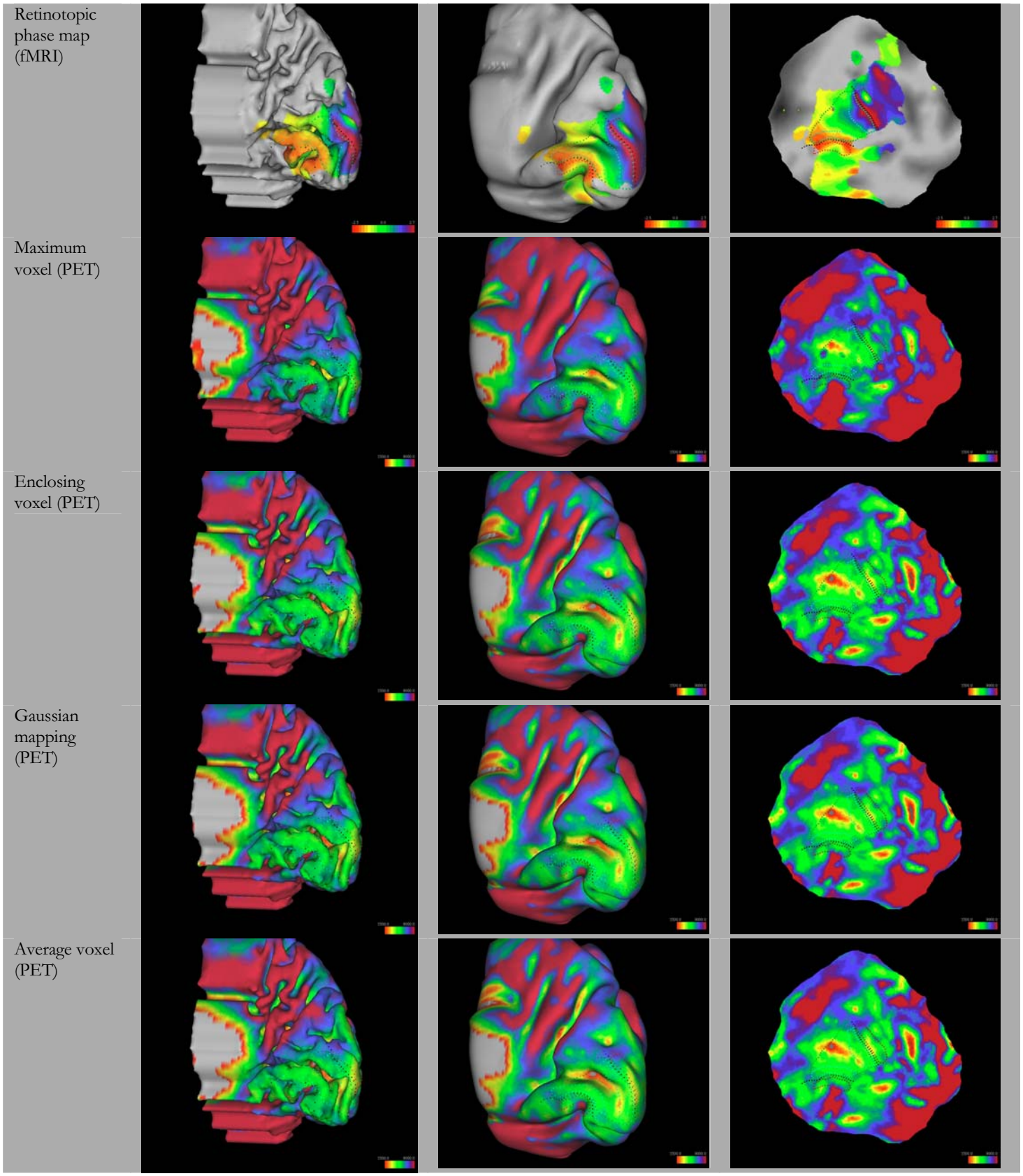

Figure 21. Functional data of one subject mapped on surface models reconstructed from subjects structural MRI scan. Column 1 shows the fiducial surface model, column 2 an inflated display while column 3 exhibits the according flattened representation.

9.4.5 Statistical analysis

Serotonin$_{1A}$ receptor binding potential (RBP) data were averaged across each region of interest (V1, V2) defined by manual delineation as described before. The ratio of average RBP between the ROIs located in V1 and V2 was calculated. Inter- and intraindividual differences in that ratio as well as variance figures of the ROI-data are presented in the Results section. Receptor density differences were tested for significance using the GNU R software (http://www.r-project.org, The R Foundation for Statistical Computing, Vienna). The employed paired t-test confirmed the results to be highly significant ($p<0.001$)

10 Results

10.1 Delineation of the primary visual cortex

The flattened representations of occipital lobes of all subjects overlayed with SNR-masked phase data are given in Figure 24 - Figure 37. Figure 22 introduces the color coding of the phase maps which is in accordance to the angular position of the wedge stimulus in the distinctive visual hemifield while Figure 23 illustrates how the delineation of V1 based on phase encoded information as described in section 9.4.4.7 was done based on the colour table from Figure 22. For facilitated orientation on the flatmap, the key anatomical landmarks are also indicated.

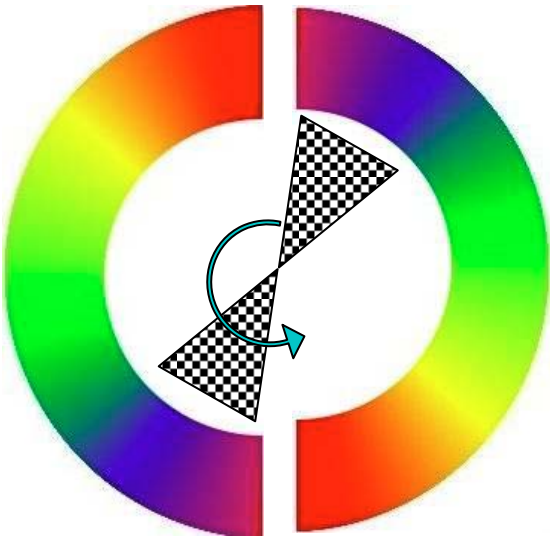

Figure 22. color table of the phasemapping. Colours are encoded according to the angular position of the visual stimulus in the respective visual hemifield. Note that the left hemifield is mapped to the RIGHT hemisphere where as the opposite is true for the right hemifield.

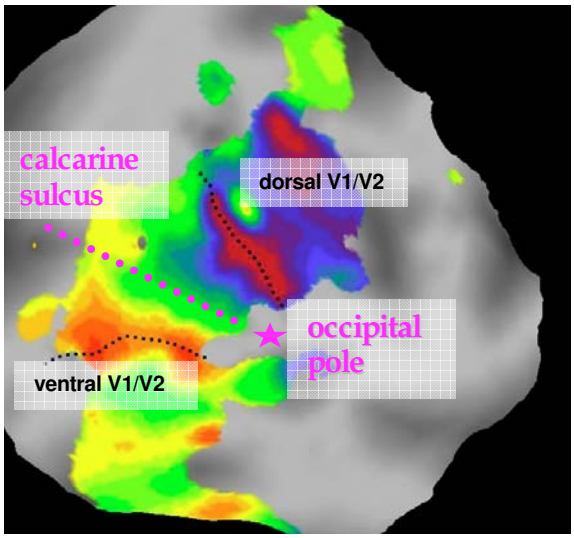

Figure 23. Right hemisphere with retinotopic phase information: the wedge stimulus rotating counterclockwise moved from the upper vertical meridian of the left visual hemifield, represented at the ventral border of V1 (red) through the horizontal meridian, located in the depth of the calcarine sulcus (green) towards the lower vertical meridian, situated at the dorsal border of V1 (purple). Accordingly, delineation was done along the minimum (red) and maximum (purple) regions indicating the ventral and dorsal V1/V2 border.

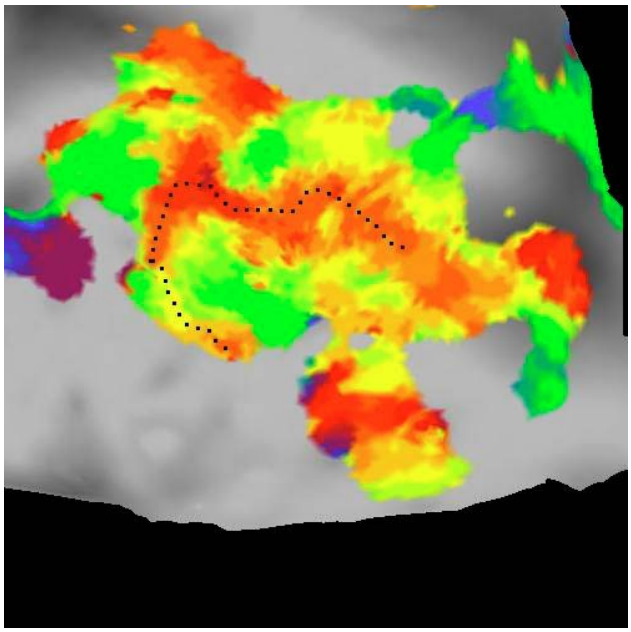

Figure 24. Subject 1, left hemisphere

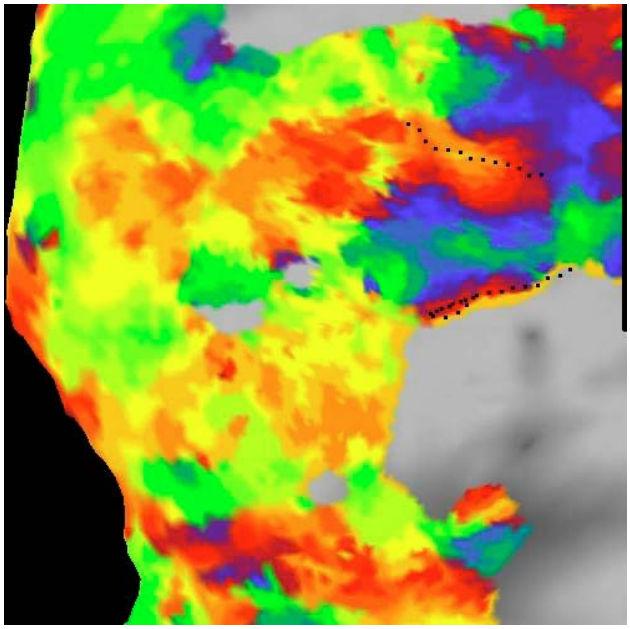

Figure 25. Subject 1, right hemisphere

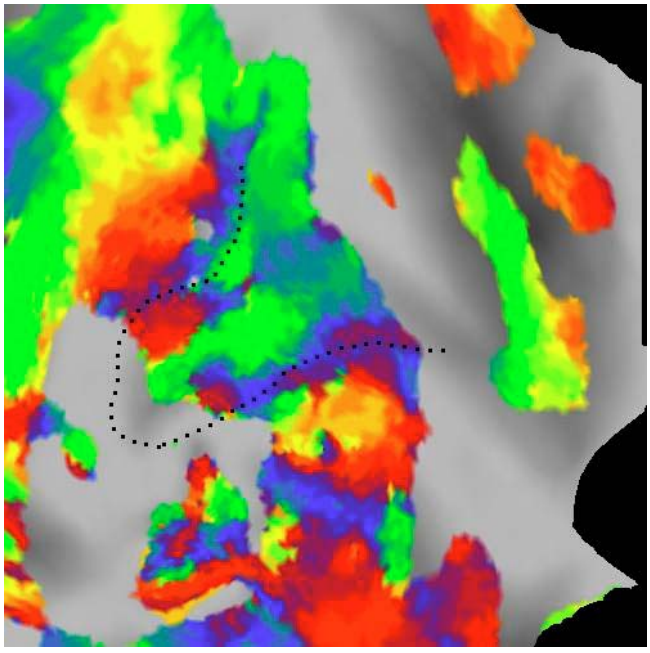

Figure 26. Subject 2, left hemisphere

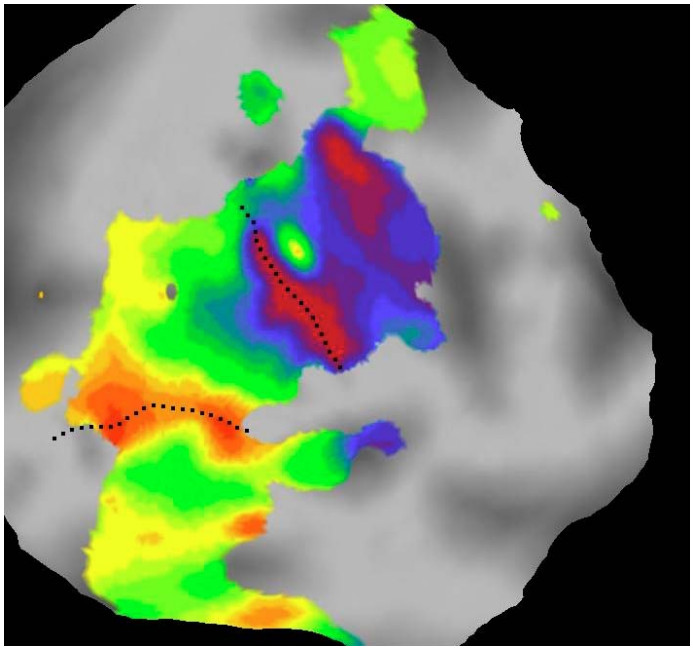

Figure 27. Subject 2, right hemisphere

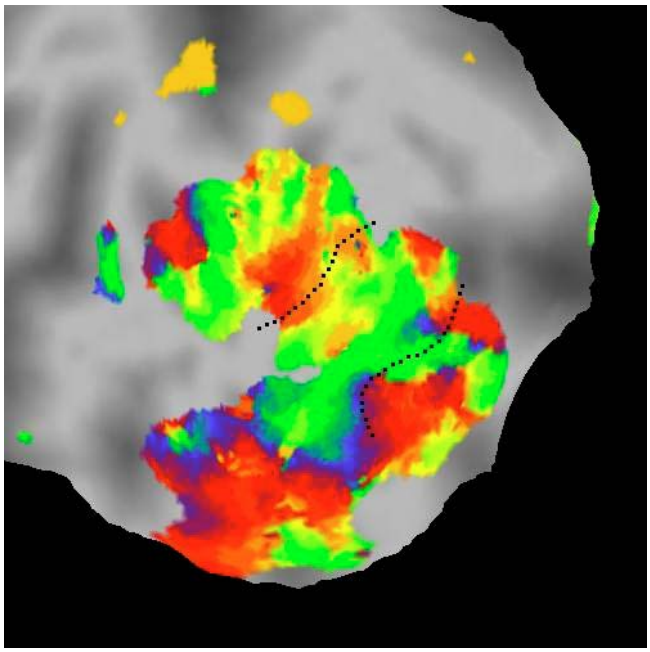

Figure 28. Subject 3, left hemisphere

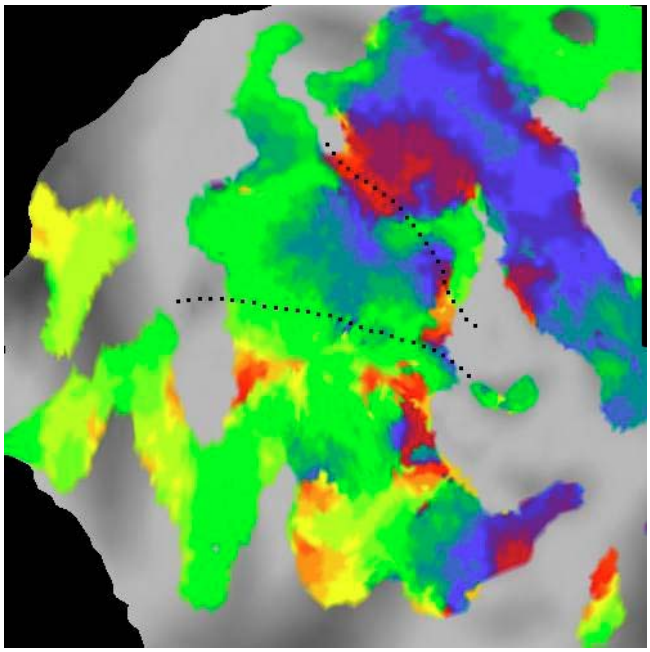

Figure 29. Subject 3, right hemisphere

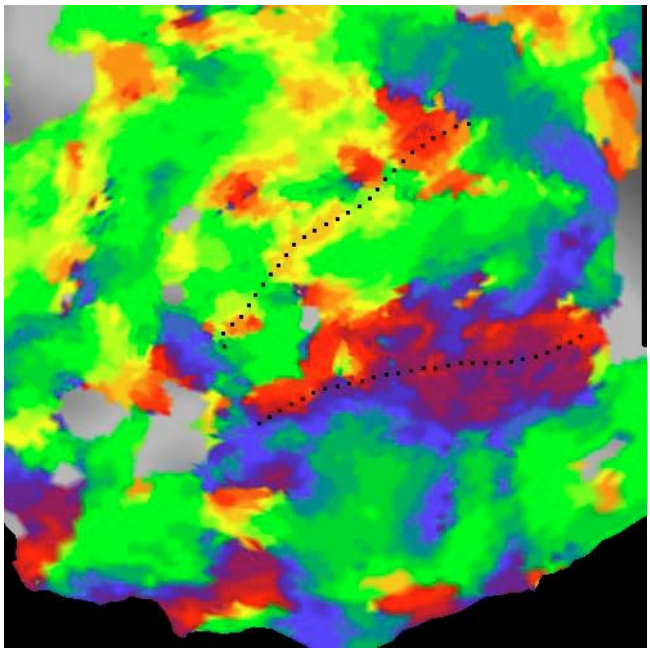

Figure 30. Subject 4, left hemisphere

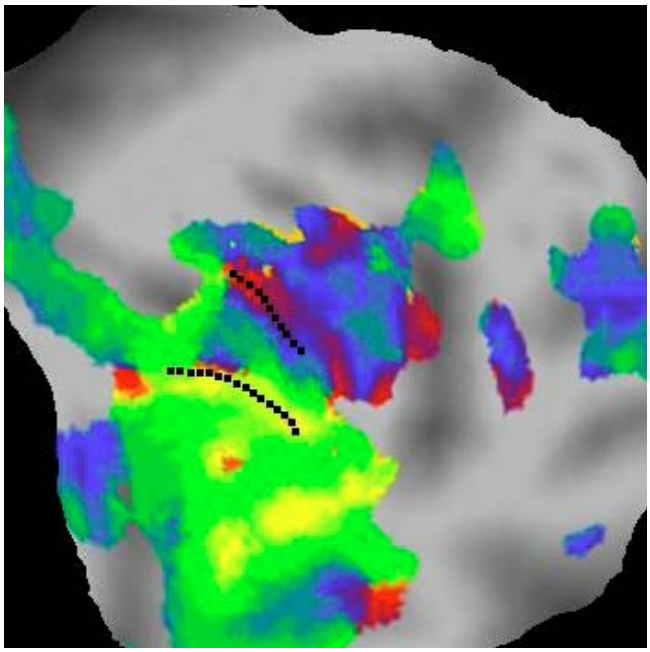

Figure 31. Subject 4, right hemisphere

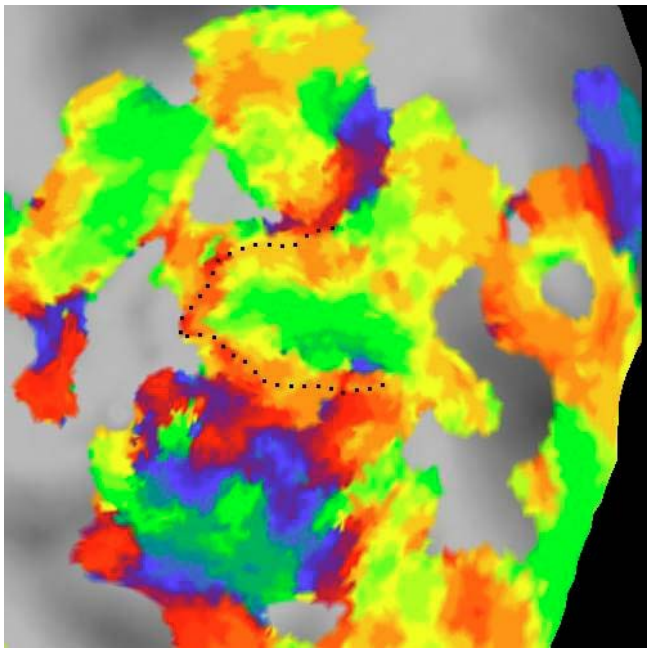

Figure 32. Subject 5, left hemisphere

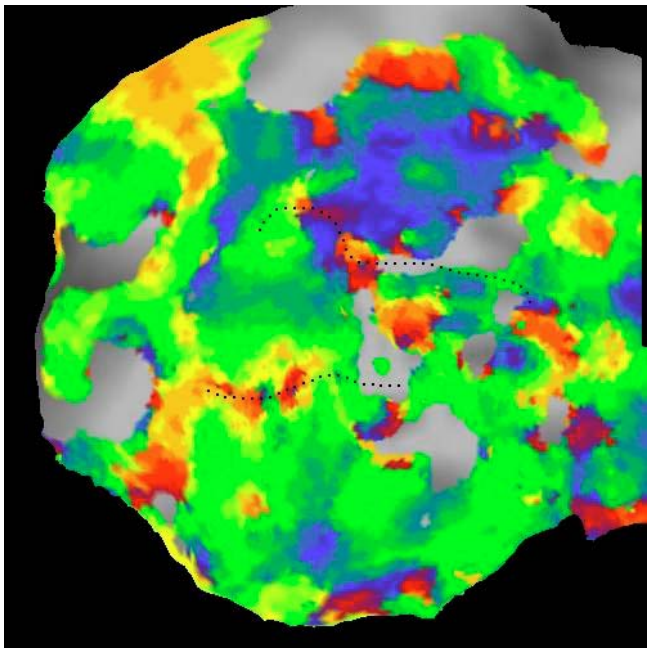

Figure 33. Subject 5, right hemisphere

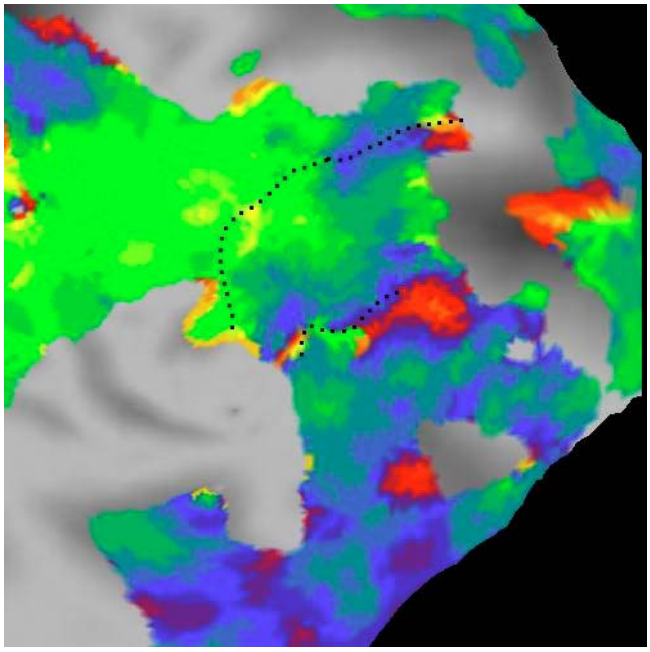

Figure 34. Subject 6, left hemisphere

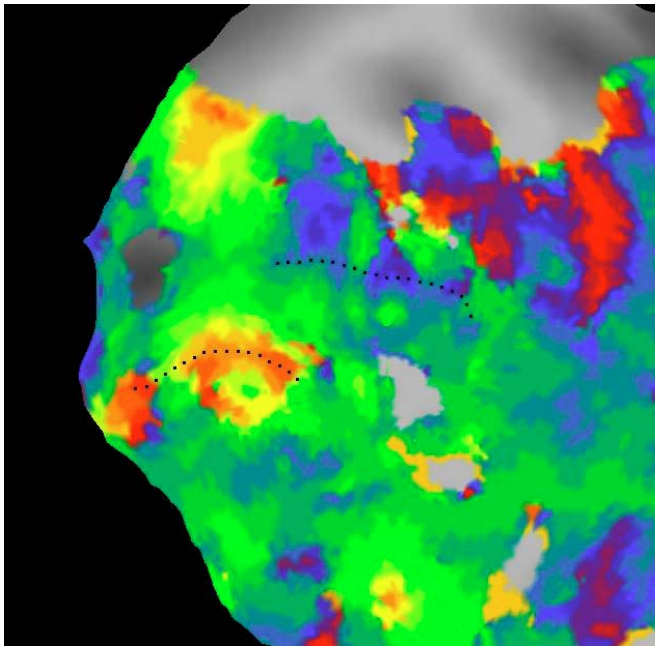

Figure 35. Subject 6, right hemisphere

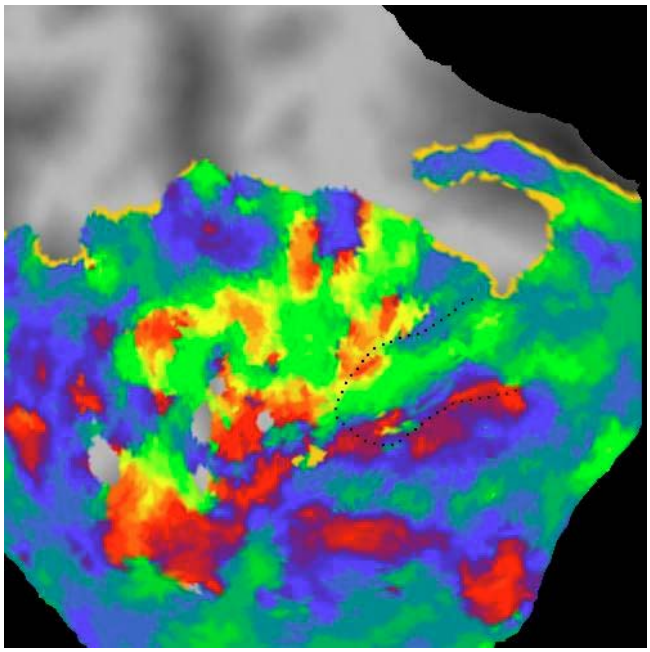

Figure 36. Subject 7, left hemisphere

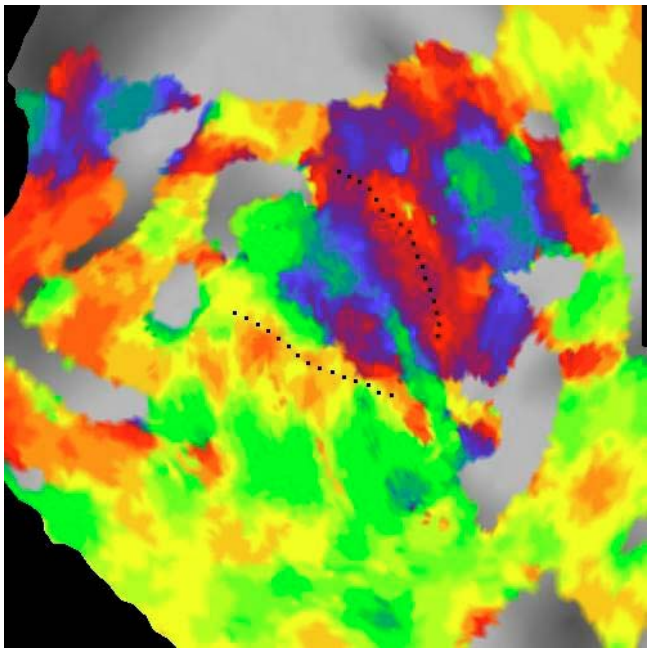

Figure 37. Subject 7, right hemisphere

10.2 Regions of interest

Region of interest sizes are limited by the extent of high quality retinotopic phase data in each subject and vary between 94 to 815 mm² for V1 and 86 to 689 mm² for V2 in the individually delineated hemispheres. Details are given in Table 6.

Subject	Hemisphere	V1 ROI(mm²)	V2 ROI (mm²)
1	Left	331	290
1	Right	441	387
2	Left	301	244
2	Right	165	237
3	Left	815	689
3	Right	334	447
4	Left	184	314
4	Right	94	86
5	Left	487	422
5	Right	408	486
6	Left	280	208
6	Right	454	631
7	Left	456	385
7	Right	317	231
Mean size	Both	362	361

Table 6. ROI sizes of manually delineated functional areas

10.3 Receptor binding potential in V1 and V2

The mean 5-HT$_{1A}$ receptor binding potential in the delineated ROIs is presented in Table 7 to Table 10. For the four different mapping algorithms differences in 5-HT$_{1A}$ receptor binding potential between primary and secondary visual cortices were shown to be significant ($p < 0.001$) for all four mapping approaches using paired T-Tests.

Assignment Method: Maximum voxel 4 mm

Subject	Hemisphere	Mean BP inV1	Sample Deviation in V1	Mean BP in Whole V1 ROI	Sample Deviation in Whole V1 ROI	Mean BP inV2	Sample Deviation in V2
1	left	2.86	0.19	2.46	0.62	3.48	0.36
1	right	3.43	1.24	2.86	0.32	4.18	0.47
2	left	1.50	0.30	1.68	0.33	2.10	0.38
2	right	1.62	0.15	1.61	0.30	1.92	0.14
3	left	1.31	0.27	1.25	0.28	1.76	0.34
3	right	1.60	0.23	1.48	0.34	1.93	0.36
4	left	2.43	0.49	2.02	0.38	2.57	0.30
4	right	1.85	0.30	1.75	0.30	2.28	0.38
5	left	0.96	0.33	0.97	0.34	1.13	0.28
5	right	0.86	0.31	0.96	0.33	1.14	0.26
6	left	2.65	0.32	2.48	0.30	2.97	0.46
6	right	1.97	0.92	2.16	0.88	2.41	0.61
7	left	1.70	0.23	1.58	0.32	1.88	0.14
7	right	1.46	0.21	1.62	0.22	1.75	0.20

Table 7. Average receptor binding potential and sample deviation mapped onto the cerebral surface model employing a 4 x 4 mm maximum voxel algorithm.

Assignment Method: Enclosing voxel mapping

Subject	Hemisphere	Mean BP inV1	Sample Deviation in V1	Mean BP in Whole V1 ROI	Sample Deviation in Whole V1 ROI	Mean BP inV2	Sample Deviation in V2
1	left	2.59	0.22	2.08	0.70	3.06	0.44
1	right	2.56	1.47	2.57	0.45	3.36	0.83
2	left	1.19	0.28	1.41	0.35	1.84	0.26
2	right	1.45	0.15	1.40	0.31	1.70	0.14
3	left	1.04	0.25	1.02	0.28	1.49	0.31
3	right	1.35	0.23	1.22	0.34	1.62	0.32
4	left	2.09	0.42	1.76	0.35	2.20	0.25
4	right	1.54	0.28	1.45	0.29	1.96	0.34
5	left	0.66	0.31	0.66	0.33	0.89	0.27
5	right	0.67	0.29	0.73	0.28	0.89	0.25
6	left	2.32	0.19	2.20	0.23	2.64	0.40
6	right	1.48	0.78	1.68	0.81	2.01	0.62
7	left	1.45	0.27	1.36	0.34	1.69	0.17
7	right	1.33	0.22	1.48	0.23	1.62	0.22

Table 8. Average receptor binding potential and sample deviation mapped onto the cerebral surface model employing an enclosing voxel algorithm

Assignment Method: Gaussian mapping

Subject	Hemisphere	Mean BP inV1	Sample Deviation in V1	Mean BP in Whole V1 ROI	Sample Deviation in Whole V1 ROI	Mean BP inV2	Sample Deviation in V2
1	left	2.58	0.21	2.08	0.69	2.98	0.42
1	right	2.49	1.43	2.57	0.42	3.33	0.82
2	left	1.21	0.29	1.42	0.35	1.83	0.24
2	right	1.46	0.14	1.41	0.31	1.70	0.11
3	left	1.05	0.23	1.02	0.27	1.47	0.29
3	right	1.36	0.22	1.22	0.34	1.60	0.29
4	left	2.06	0.38	1.75	0.34	2.18	0.21
4	right	1.58	0.26	1.48	0.27	1.92	0.30
5	left	0.65	0.27	0.64	0.30	0.87	0.24
5	right	0.67	0.27	0.73	0.26	0.89	0.23
6	left	2.35	0.21	2.19	0.24	2.62	0.38
6	right	1.47	0.74	1.68	0.77	2.00	0.60
7	left	1.46	0.25	1.36	0.34	1.70	0.15
7	right	1.34	0.22	1.48	0.22	1.62	0.21

Table 9. Average receptor binding potential and sample deviation mapped onto the cerebral surface model employing a Gaussian mapping algorithm, 4mm bounding box, surface normal σ: 4mm, surface tangent σ: 4mm, above surface cutoff: 1mm algorithm

Assignment Method: Average voxel mapping

Subject	Hemisphere	Mean BP inV1	Sample Deviation in V1	Mean BP in Whole V1 ROI	Sample Deviation in Whole V1 ROI	Mean BP inV2	Sample Deviation in V2
1	left	2.58	0.21	2.08	0.68	3.01	0.42
1	right	2.57	1.38	2.57	0.42	3.33	0.75
2	left	1.21	0.27	1.42	0.33	1.80	0.25
2	right	1.44	0.15	1.40	0.30	1.68	0.13
3	left	1.06	0.24	1.02	0.27	1.48	0.29
3	right	1.35	0.21	1.22	0.32	1.60	0.31
4	left	2.08	0.38	1.76	0.33	2.21	0.21
4	right	1.57	0.26	1.47	0.28	1.95	0.30
5	left	0.66	0.28	0.66	0.30	0.87	0.23
5	right	0.66	0.26	0.73	0.26	0.89	0.23
6	left	2.33	0.19	2.19	0.22	2.60	0.37
6	right	1.48	0.75	1.69	0.78	2.02	0.59
7	left	1.46	0.24	1.37	0.33	1.68	0.16
7	right	1.34	0.22	1.48	0.22	1.62	0.21

Table 10 Average receptor binding potential and sample deviation mapped onto the cerebral surface model employing an algorithm averaging over a 4mm box

The receptor density ratios between the extended V1 ROI (wV1) and the V2 ROI are presented in Table 11 for all four applied mapping algorithms.

Subject	Hemisphere	Maximum voxel	Enclosing voxel	Gaussian mapping	Average voxel
1	left	0.82	0.85	0.87	0.86
1	right	0.82	0.76	0.75	0.77
2	left	0.72	0.65	0.66	0.67
2	right	0.85	0.85	0.85	0.86
3	left	0.75	0.70	0.72	0.71
3	right	0.83	0.83	0.85	0.85
4	left	0.95	0.95	0.94	0.94
4	right	0.81	0.79	0.82	0.81
5	left	0.85	0.74	0.74	0.76
5	right	0.75	0.75	0.75	0.75
6	left	0.90	0.88	0.90	0.89
6	right	0.82	0.73	0.74	0.74
7	left	0.91	0.86	0.86	0.87
7	right	0.83	0.82	0.83	0.83

Table 11. Effect of different mapping algorithms on the V1 / V2 ratio

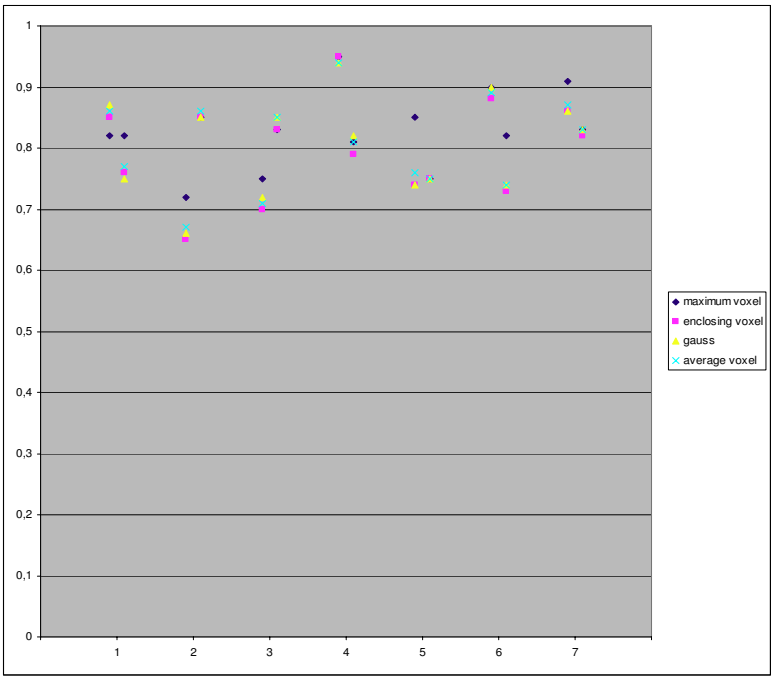

Figure 38 Illustration of the effects of different mapping algorithms on the V1 / V2 ratio

The receptor density ratios between the extended V1 ROI (wV1) and the V2 ROI are presented in Table 12 for all four applied mapping algorithms

Subject	Hemisphere	Maximum voxel	Enclosing voxel	Gaussian mapping	Average voxel
1	left	0.71	0.68	0.70	0.69
1	right	0.68	0.76	0.77	0.77
2	left	0.80	0.77	0.78	0.79
2	right	0.84	0.82	0.82	0.84
3	left	0.71	0.69	0.69	0.69
3	right	0.77	0.75	0.76	0.76
4	left	0.79	0.80	0.80	0.80
4	right	0.77	0.74	0.77	0.76
5	left	0.85	0.74	0.74	0.76
5	right	0.84	0.82	0.82	0.82
6	left	0.83	0.83	0.84	0.84
6	right	0.90	0.84	0.84	0.84
7	left	0.84	0.81	0.80	0.81
7	right	0.92	0.91	0.91	0.92

Table 12 Effect of different mapping algorithms on the extended V1 / V2 ratio

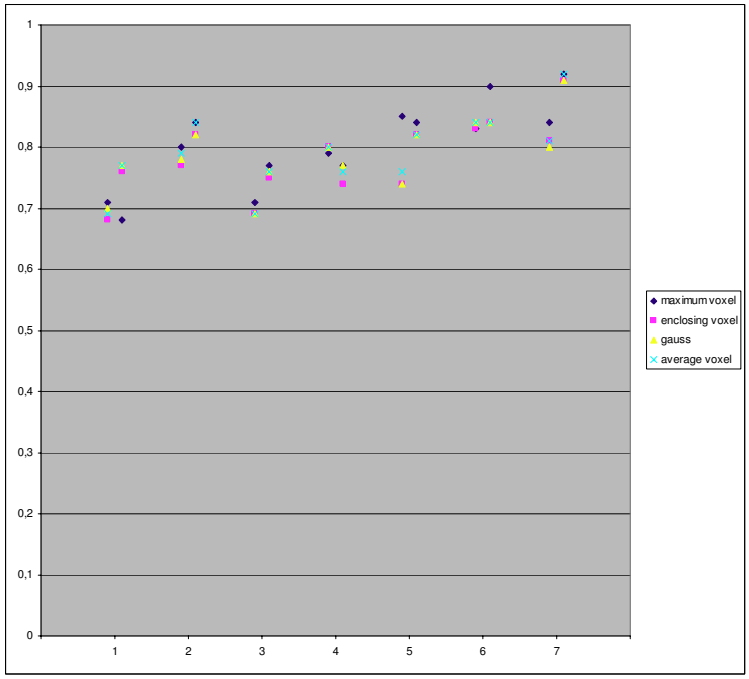

Figure 39 Illustration of the effects of different mapping algorithms on the V1 / V2 ratio

A comparison of the ratios resulting from the two different V1 ROIs is visualized in Figure 40

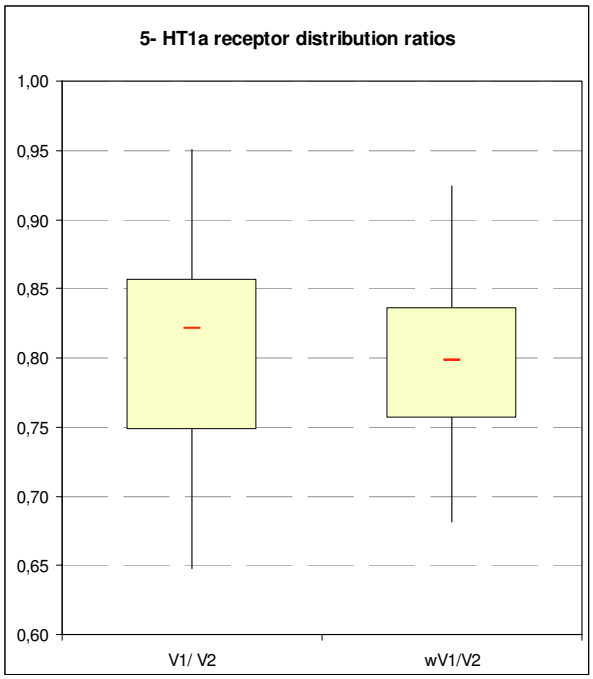

Figure 40. Box plot of receptor distribution ratios indicating minimum, maximum values as whiskers, the box area is demarcated by the 25% and 75% percentile and the median is indicated as red line in the box

Table 13 summarizes the average ratios between the twofold delineated V1 and V2.. Since seven subjects with 2 hemispheres and 2 different v1 ROIs were compared employing 4 different PET mappings each a total of 112 V1/V2 ratios resulted. The frequency distribution of all 112 ratios is shown in Figure 41 and illustrates the denoted ratio of 0.8

	V1/V2	StDev V1/V2	V1whole/V2	StDev wV1/V2
Maximum Voxel 4mm	0.83	0.06	0.80	0.07
Enclosing Voxel	0.80	0.08	0.78	0.06
Gaussian kernel 4mm	0.80	0.08	0.79	0.06
Average Voxel 4mm	0.81	0.08	0.79	0.06

Table 13 Comparison of mean receptor-distribution ratios achieved by different mapping algorithms

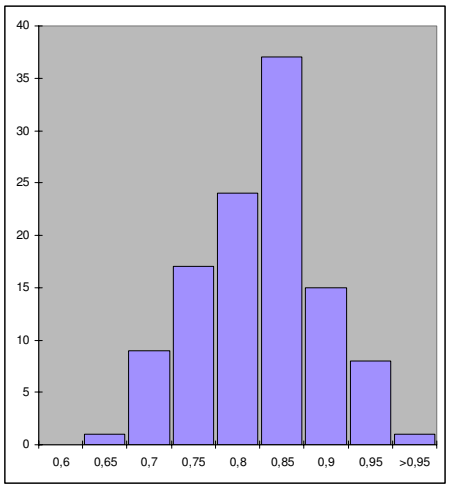

Figure 41 Histogram of all 112 calculated V1/V2 receptor ratios

.

11 Discussion

In this multimodal imaging study for the first time the ratio of neurotransmitter distribution between sensory areas of same modality but distinct hierarchy *in vivo* was investigated. This assessment was done for the human visual network in the study at hand. Systematic differences of receptor distribution patterns between hierarchies of a cortical network has been described for the motor system of macaque monkeys (Geyer, Matelli et al. 1998), somatosensory areas in macaques and humans (Mash, White et al. 1988; Geyer, Schleicher et al. 1997; Zilles, Palomero-Gallagher et al. 2002) only in autoradiographic post-mortem studies up till now.

Examining seven subjects with two regions of interest in each hemisphere, V1 being delineated twice focusing on different aspects and employing four different approaches of mapping neurochemical data to the cortical surface model, a total of 112 ratios of 5-HT$_{1A}$ receptor distributions between primary and secondary visual cortex was reckoned. As presented in the results section of this thesis the ratios between the primary and secondary visual cortices follow a normal distribution with *0.8* as central value. This is in very good agreement with the ratio of *0.57* as found by the post-mortem study of Scheperjans et al., to our knowledge the only published study presenting receptor distribution data for distinct areas of the visual cortex (Scheperjans, Palomero-Gallagher et al. 2005). The ratio of *0.57* was derived from quantitative autoradiographical data averaging the values from three areas of V2 located at different locations at the cerebral cortex and comparing it with the V1

value estimated around the calcarine sulcus (thanks to Filip Scheperjans for providing the data in personal communication).

A methodological limitation of quantitative PET imaging is that the spatial resolution achievable lies around 5 millimetres. This leads to spillover effects between areas that exhibit different distributions of the radioligand's target. In contrast, post-mortem methods using autoradiography with radiotracers allow for inplane resolutions of 30µm x 30µm on brain slices, exhibiting even laminar distribution patterns of a given receptor (Zilles, Palomero-Gallagher et al. 2002; Scheperjans, Palomero-Gallagher et al. 2005). When utilizing the latter method of post-mortem autoradiography as a reference in an *in-vivo* comparison of the receptor distribution in two neighbouring areas the effects described above necessarily lead towards a smaller difference in the PET method. This attenuated difference compared to the post-mortem "gold standard" is reflected in this study's finding of a ratio of *0.8* between V1 and V2 for the distribution of the 5-HT$_{1A}$ receptor compared to the ratio of *0.57* from autoradiographical examination.

While cortical surface-based analysis is a well established method in functional magnetic resonance imaging studies of the cerebral cortex, likewise processing of data acquired by positron emission tomography is sparsely described in literature (Park, Lee et al. 2006). No surface-based *in vivo* analysis of 5-HT$_{1A}$ receptor binding in the cerebral cortex of humans has, however been reported until today. To assess the effects of different receptor density mapping algorithms on the V1/V2 ratio we therefore utilized four different mapping algorithms.

Mapping the highest measured 5-HT$_{1A}$ binding potential within a 4 mm³ box to a node of the cortical surface model employing the maximum voxel algorithm resulted,

as expected, in the mappings most diverging from the rest, but nevertheless the results were in excellent agreement with our overall findings. Further research in the field of surface based visualisation and analysis of data achieved by molecular imaging methods seems to be promising, considering the general beneficial effects surface based analysis yields for other imaging modalities like fMRI, as well as improvements that may be advantageous for PET imaging in particular such as the correction for partial voluming effects that can be realized employing the surface-based approach (Park, Lee et al. 2006).

The twofold delineation of regions of interest in the primary visual cortex was performed to obtain information about the situation of the bordering region between V1 and V2 (limiting the V1 ROI to areas close to this border), while on the other hand considering the neurochemical situation within the whole extent of delineated V1 (including all of the retinotopically defined V1 in the ROI).

A further point of consideration is the average age of the brains analyzed. The mean age of the brains in the study cited as reference was 71.8 years compared to an average age of 24.4 in our study group. Age related decreases in receptor density have been reported for several types including 5-HT$_{1A}$, where receptor density is described to decline by approximately 10% per decade of life (Dillon, Gross-Isseroff et al. 1991; Tauscher, Verhoeff et al. 2001). Other studies, then again, question this age related decline. Rabiner et al. find no age related 5-HT$_{1A}$ receptor binding potential decline within an age range of 24-53 years (Rabiner, Messa et al. 2002). Consequently, the influence of age on neurotransmitter receptor density may be regarded as an issue of ongoing debate. It seems, however, fairly unlikely that a supposed effect of the mentioned kind would alter the ratio of 5-HT$_{1A}$ receptor distribution between various functional areas of the visual cortex.

Several studies report an influence of steroid hormone levels on the expression of the 5-HT$_{1A}$ receptor but this influence appears to play only a minor role in the occipital cortex (Bethea, Lu et al. 2002; Parsey, Oquendo et al. 2002) and thus are not to be expected to notably effect comparisons within this region.

Functional fields themselves do not exhibit a homogeneous density but rather show variation in neurotransmitter receptor distribution within their borders. As hypothesized by (Scheperjans, Palomero-Gallagher et al. 2005) in the visual system this variation may well occur due to visual processing in early cortical areas, which changes within these areas with the distance to the foveal representation (Harris and Fahle 1996). Thus, inhomogenieties in neurotransmitter receptor distribution may reveal further functional segregation. Given the considerable variation that may occur within a functional area, and methodological limitations in PET imaging related especially to spatial resolution the issue of how reliable borders can be identified by means of this method remains to be further evaluated.

One important constraint for the possible extension of the applied method to other cortical areas arises from findings from the cited post-mortem studies: The quantification of one receptor type alone was not sufficient for a delineation of all cortical areas. Rather, quantification using many neurochemical markers resulted in characteristic patterns of neurotransmitter receptor densities, which are referred to as "receptor fingerprints" (Zilles, Palomero-Gallagher et al. 2002). The application of numerous PET scans in one subject seems not viable for financial, practical and ethical reasons. Therefore, addressing the issue of which borders can be as securely assessed by which neurochemical marker, as it is the case with the 5-HT$_{1A}$ receptor in the visual cortex, remains a matter of future research.

Nevertheless, we consider the assessment of data resulting from molecular imaging methods, in particular positron emission tomography, within distinct hierarchical areas of a functional system as an essential initial step towards applying neurochemical criteria for the parcellation of the living brain. These neurochemical parameters provide, as exemplified in this thesis, valuable insight on underlying functional properties of the sensory system.

A generalization of our results to other areas of the brain may provide a completely new approach towards brain mapping, postulating in conformity with the post-mortem data available (Zilles, Palomero-Gallagher et al. 2002) that the tight relationship between function and receptor distribution patterns, here demonstrated for the visual system, exists for the whole brain.

12 Conclusion

The data resulting from this study clearly supports the assumption that the 5-HT$_{1A}$ receptor distribution pattern can be used to define the primary visual cortex by a neurochemical marker in humans in vivo. This finding is consistent with post-mortem examinations addressing this specific issue (Zilles, Palomero-Gallagher et al. 2002; Scheperjans, Palomero-Gallagher et al. 2005).

By demonstrating in principle the viability of PET imaging as a means of parcellation of the cortical surface, verified by well established principles of functional magnetic resonance imaging and retinotopic mapping procedures, we made an important first step towards reversing the approach of interpreting molecular imaging data on grounds of prior parcellation employed by numerous other studies.

From our point of view, the possibility of performing cortical parcellation on the basis of neurochemical distribution patterns yields numerous promising possibilities, for instance in the further exploration of sensory areas in absence of their specific input or the investigation of functional regions not accessible by current fMRI paradigms.

Concluding from this outlook, this method may well prove as a valuable tool in the exploration of the physiological as well as pathological functioning of the human brain.

13 Figures

14 Tables

15 Abbreviations

5-HT	Serotonin
5-HT$_{1A}$	Serotonin-1A receptor
B_{max}	Maximum concentration of binding sites
BOLD	blood oxygen level dependent
CARET	Computerized Anatomical Reconstruction and Editing Toolkit (software)
CBF	cerebral blood flow
CBV	cerebral blood volume
CNR	contrast/noise ratio (CNR = ($signal_A$ - $signal_B$) / noise)
Ci	Curie (1 Ci = 3.7×10^{10} decays per second.)
f2	Free fraction of the unbound tracer
fi	Free fraction of the competing endogenous ligand
FWHM	Full Width at Half Maximum
IDL	Interactive data language (software)
K_i	Dissociation constants for the competing endogenous ligand
MBq	Megabecquerel
MeV	Megaelectronvolt
MOG	mixture of Gaussians model
MRI	Magnetic resonance imaging
PET	Positron Emission Tomography
ROI	Region of interest
SNR	signal/noise ratio
SPM	statistical parametric mapping
SRTM	Simplified Reference Tissue Model
TE	echo time
TR	repetition time

16 References

Adams, D. L. and J. C. Horton (2003). "A precise retinotopic map of primate striate cortex generated from the representation of angioscotomas." J Neurosci **23**(9): 3771-89.

Amunts, K., A. Malikovic, et al. (2000). "Brodmann's areas 17 and 18 brought into stereotaxic space-where and how variable?" Neuroimage **11**(1): 66-84.

Ashburner, J. and K. J. Friston (2005). "Unified segmentation." Neuroimage **26**(3): 839-51.

Baldwin, D. and S. Rudge (1995). "The role of serotonin in depression and anxiety." Int Clin Psychopharmacol **9 Suppl 4**: 41-5.

Bethea, C. L., N. Z. Lu, et al. (2002). "Diverse actions of ovarian steroids in the serotonin neural system." Front Neuroendocrinol **23**(1): 41-100.

Bridge, H., S. Clare, et al. (2005). "Independent anatomical and functional measures of the V1/V2 boundary in human visual cortex." J Vis **5**(2): 93-102.

Brodmann, K. (1909). Vergleichende Lokalisationslehre der Grosshirnrinde : in ihren Prinzipien dargestellt auf Grund des Zellenbaues. Leipzig, Barth.

Buhot, M. C., S. Martin, et al. (2000). "Role of serotonin in memory impairment." Ann Med **32**(3): 210-21.

DeYoe, E. A., G. J. Carman, et al. (1996). "Mapping striate and extrastriate visual areas in human cerebral cortex." Proc Natl Acad Sci U S A **93**(6): 2382-6.

Dillon, K. A., R. Gross-Isseroff, et al. (1991). "Autoradiographic analysis of serotonin 5-HT1A receptor binding in the human brain postmortem: effects of age and alcohol." Brain Res **554**(1-2): 56-64.

Drury, H. A., D. C. Van Essen, et al. (1996). "Computerized mappings of the cerebral cortex: a multiresolution flattening method and a surface-based coordinate system." J Cogn Neurosci **8**(1): 1-28.

Dumoulin, S. O., R. D. Hoge, et al. (2003). "Automatic volumetric segmentation of human visual retinotopic cortex." Neuroimage **18**(3): 576-87.

Engel, S. A., G. H. Glover, et al. (1997). "Retinotopic organization in human visual cortex and the spatial precision of functional MRI." Cereb Cortex **7**(2): 181-92.

Engel, S. A., D. E. Rumelhart, et al. (1994). "fMRI of human visual cortex." Nature **369**(6481): 525.

Felleman, D. J. and D. C. Van Essen (1991). "Distributed hierarchical processing in the primate cerebral cortex." Cereb Cortex **1**(1): 1-47.

Geyer, S., M. Matelli, et al. (1998). "Receptor autoradiographic mapping of the mesial motor and premotor cortex of the macaque monkey." J Comp Neurol **397**(2): 231-50.

Geyer, S., A. Schleicher, et al. (1997). "The somatosensory cortex of human: cytoarchitecture and regional distributions of receptor-binding sites." Neuroimage **6**(1): 27-45.

Gunn, R. N., P. A. Sargent, et al. (1998). "Tracer kinetic modeling of the 5-HT1A receptor ligand [carbonyl-11C]WAY-100635 for PET." Neuroimage **8**(4): 426-40.

Halldin, C., B. Gulyas, et al. (2001). "PET studies with carbon-11 radioligands in neuropsychopharmacological drug development." Curr Pharm Des **7**(18): 1907-29.

Hamon, M., L. Lanfumey, et al. (1990). "The main features of central 5-HT1 receptors." Neuropsychopharmacology **3**(5-6): 349-60.

Harris, J. P. and M. Fahle (1996). "Differences between fovea and periphery in the detection and discrimination of spatial offsets." Vision Res **36**(21): 3469-77.

Heiss, W. D. and K. Herholz (2006). "Brain receptor imaging." J Nucl Med **47**(2): 302-12.

Kasper S, Tauscher J, Willeit M, Stamenkovic M, Neumeister A, Küfferle B, Barnas C, Stastny J, Praschak-Rieder N, Pezawas L, de Zwaan M, Quiner S, Pirker W, Asenbaum S, Podreka I, Brücke T (2002). "Receptor and transporter imaging studies in schizophrenia, depression, bulimia and Tourette's disorder--implications for psychopharmacology." World J Biol Psychiatry **3**(3): 133-46.

Kwong, K. K., J. W. Belliveau, et al. (1992). "Dynamic magnetic resonance imaging of human brain activity during primary sensory stimulation." Proc Natl Acad Sci U S A **89**(12): 5675-9.

Lammertsma, A. A. and S. P. Hume (1996). "Simplified reference tissue model for PET receptor studies." Neuroimage **4**(3 Pt 1): 153-8.

Lanzenberger, R. R., M. Mitterhauser, et al. (2007). "Reduced serotonin-1A receptor binding in social anxiety disorder." Biol Psychiatry **61**(9): 1081-9.

Mash, D. C., W. F. White, et al. (1988). "Distribution of muscarinic receptor subtypes within architectonic subregions of the primate cerebral cortex." J Comp Neurol **278**(2): 265-74.

Matarrese, M., F. Sudati, et al. (2002). "Automation of [11C]acyl chloride syntheses using commercially available 11C-modules." Appl Radiat Isot **57**(5): 675-9.

Muehllehner, G. and J. S. Karp (2006). "Positron emission tomography." Phys Med Biol **51**(13): R117-37.

Ogawa, S., T. M. Lee, et al. (1990). "Brain magnetic resonance imaging with contrast dependent on blood oxygenation." Proc Natl Acad Sci U S A **87**(24): 9868-72.

Park, H. J., J. D. Lee, et al. (2006). "Cortical surface-based analysis of 18F-FDG PET: measured metabolic abnormalities in schizophrenia are affected by cortical structural abnormalities." Neuroimage **31**(4): 1434-44.

Parsey, R. V., M. A. Oquendo, et al. (2002). "Effects of sex, age, and aggressive traits in man on brain serotonin 5-HT1A receptor binding potential measured by PET using [C-11]WAY-100635." Brain Res **954**(2): 173-82.

Pike, V. W., J. A. McCarron, et al. (1996). "Exquisite delineation of 5-HT1A receptors in human brain with PET and [carbonyl-11 C]WAY-100635." Eur J Pharmacol **301**(1-3): R5-7.

Qiu, F. T. and R. von der Heydt (2005). "Figure and ground in the visual cortex: v2 combines stereoscopic cues with gestalt rules." Neuron **47**(1): 155-66.

Rabiner, E. A., C. Messa, et al. (2002). "A database of [(11)C]WAY-100635 binding to 5-HT(1A) receptors in normal male volunteers: normative data and relationship to methodological, demographic, physiological, and behavioral variables." Neuroimage **15**(3): 620-32.

Rapport, M. M., A. A. Green, et al. (1948). "SERUM VASOCONSTRICTOR (SEROTONIN). IV. ISOLATION AND CHARACTERIZATION." J. Biol. Chem. **176**(3): 1243-1251.

Scheperjans, F., N. Palomero-Gallagher, et al. (2005). "Transmitter receptors reveal segregation of cortical areas in the human superior parietal cortex: relations to visual and somatosensory regions." Neuroimage **28**(2): 362-79.

Sereno, M. I., A. M. Dale, et al. (1995). "Borders of multiple visual areas in humans revealed by functional magnetic resonance imaging." Science **268**(5212): 889-93.

Shih, J. C., W. Yang, et al. (1991). "Molecular biology of serotonin (5-HT) receptors." Pharmacol Biochem Behav **40**(4): 1053-8.

Struder, H. K. and H. Weicker (2001). "Physiology and pathophysiology of the serotonergic system and its implications on mental and physical performance. Part I." Int J Sports Med **22**(7): 467-81.

Talairach, J. and P. Tournoux (1988). Co-planar stereotaxic atlas of the human brain : 3-dimensional proportional system ; an approach to medical cerebral imaging. Stuttgart ; New York
New York, G. Thieme ;
Thieme Medical Publishers.

Tauscher, J., N. P. Verhoeff, et al. (2001). "Serotonin 5-HT1A receptor binding potential declines with age as measured by [11C]WAY-100635 and PET." Neuropsychopharmacology **24**(5): 522-30.

Tootell, R. B., N. K. Hadjikhani, et al. (1998). "Functional analysis of primary visual cortex (V1) in humans." Proc Natl Acad Sci U S A **95**(3): 811-7.

Tosun, D., M. E. Rettmann, et al. (2004). "Cortical surface segmentation and mapping." Neuroimage **23 Suppl 1**: S108-18.

Turner, M. R., E. A. Rabiner, et al. (2005). "[11C]-WAY100635 PET demonstrates marked 5-HT1A receptor changes in sporadic ALS." Brain **128**(Pt 4): 896-905.

Van Essen, D. C., D. Dierker, et al. (2006). "Symmetry of cortical folding abnormalities in Williams syndrome revealed by surface-based analyses." J Neurosci **26**(20): 5470-83.

Van Essen, D. C., H. A. Drury, et al. (2001). "An integrated software suite for surface-based analyses of cerebral cortex." J Am Med Inform Assoc **8**(5): 443-59.

Van Essen, D. C., H. A. Drury, et al. (1998). "Functional and structural mapping of human cerebral cortex: solutions are in the surfaces." Proc Natl Acad Sci U S A **95**(3): 788-95.

Varnas, K., C. Halldin, et al. (2004). "Autoradiographic distribution of serotonin transporters and receptor subtypes in human brain." Hum Brain Mapp **22**(3): 246-60.

Villringer, A. and U. Dirnagl (1999). "[Pathophysiology of cerebral ischemia]." Z Arztl Fortbild Qualitatssich **93**(3): 164-8.

Wadsak (2007). "Simple and fully automated preparation of [carbonyl-11C]WAY-100635." Radiochimica Acta **95**(7): 417-422.

Warnking, J., M. Dojat, et al. (2002). "fMRI retinotopic mapping--step by step." Neuroimage **17**(4): 1665-83.

Wohlschlager, A. M., K. Specht, et al. (2005). "Linking retinotopic fMRI mapping and anatomical probability maps of human occipital areas V1 and V2." Neuroimage **26**(1): 73-82.

Zilles, K., N. Palomero-Gallagher, et al. (2002). "Architectonics of the human cerebral cortex and transmitter receptor fingerprints: reconciling functional neuroanatomy and neurochemistry." Eur Neuropsychopharmacol **12**(6): 587-99.